Noise characterisation of SiPMs from different manufacturers for CBM RICH detector

Bachelor-Thesis
for the award of the academic degree of
Bachelor of science
in the physics degree program

Faculty of Mathematics and Natural Sciences
Bergische Universität Wuppertal

handed in by:

Jan Hendrik Lietz 1922360

Supervisors:

Prof. Dr. Karl-Heinz Kampert
First Supervisor

Prof. Dr. Christian Zeitnitz
Second Supervisor

July 1, 2024

Abstract

In this bachelor thesis a detailed characterisation for the silicon photomultipliers (SiPMs) AF-BRS4N66P024 manufactured by Broadcom, MICROFC-60035 manufactured by OnSemi and S14160-6050CS manufactured by Hamamatsu is carried out. For these measurements, the SiPMs are shielded from ambient light and their temperature is kept constant at certain values, and different bias voltages are applied. The Dark Count Rate (DCR), crosstalk, afterpulse and gain are then measured for different temperatures and bias voltages. All results are discussed together in view of the selection a SiPM candidate for future development towards installing it in the Ring Imaging Cherenkov Detector (RICH) at the Compressed Baryonic Matter (CBM) experiment at the FAIR facility in Darmstadt.

Contents

List of Figures

List of Tables

1 Motivation

The aim of this thesis is to characterize different silicon photomultipliers (SiPMs) from different manufacturers in relation to their individual gain, Dark Count Rate, crosstalk, and afterpulsing. For this purpose, the SiPM models AFBR-S4N66P024 manufactured by Broadcom, MICROFC-60035 manufactured by OnSemi, and S14160-6050HS manufactured by Hamamatsu are considered. These findings will be used in a possible upgrade the Ring Imaging Cherenkov detector (RICH) at the Compressed Baryonic Matter (CBM) experiment located at GSI Darmstadt. Currently, the RICH-detector is planned to be equipped with multi-anode photo multiplier (MAPMT) tubes, The possibility of replacing all or parts of these with SiPMs as part of a future detector approach is being considered. SiPMs provide advantages in the time resolution, have potentially smaller granularity and pixel size, and have advantages also concerning the availability in the future. Radiation that hits a photomultiplier generates photoelectrons, which are multiplied to a measurable output charge. This output charge is converted into an output voltage via a series resistor. A relationship can then be established between the number of incident photons and the voltage generated. This results in a ratio of how many electrons are generated per incident photon, which is referred to as the gain. If a silicon photomultiplier generates electrons that do not result from an incoming photon, this is referred to as Dark Count Rate (DCR). These electrons usually have a thermal origin. Since the SiPMs used to consist of several microcells, Crosstalk also occurs as a result. It is caused by electrons that are generated in one cell by an incoming photon and generate another signal in a neighboring cell. There can be several reasons for this, which lie in the structure of SiPMs. To characterize the SiPMs, the DCR and crosstalk values for the different SiPMs are determined and compared.

2 CBM Physics Overview

The Compressed Baryonic Matter (CBM) experiment is an important component of the future Facility for Antiproton and Ion Research (FAIR) in Darmstadt. It will use high-energy nuclear-nuclear collisions to study the phase diagram of strongly interacting baryonic matter (Figure 1).

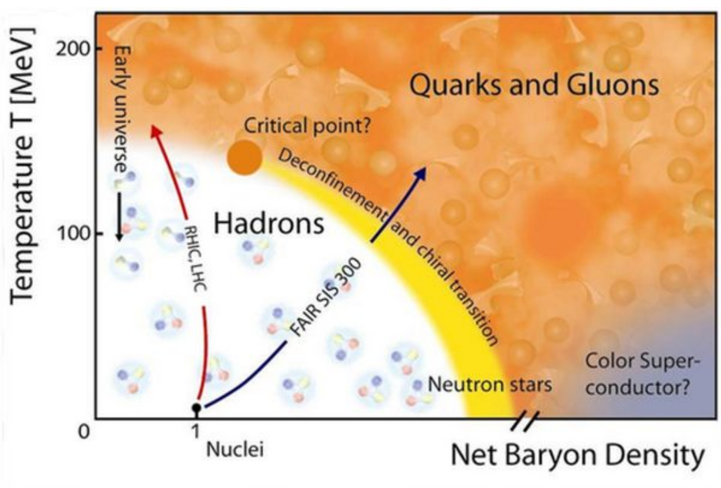

Figure 1: Hadronic phase diagram [9].

Quantum Chromodynamics (QCD) stands as the fundamental theory governing strong interactions. Its essence lies in quarks and gluons, elusive entities that resist isolation. Instead, they coalesce under normal conditions, bound by the strong interaction to form protons and neutrons, the elemental constituents of observed atomic nuclei, along with many of other hadrons. However, if the temperature or the baryon density is high enough, this strong interaction weakens, rendering interactions feeble and preventing particle cohesion. These circumstances materialize either under the temperatures of the early universe post Big Bang or in regions of exceedingly high matter density, such as within neutron stars. Here, nuclear matter transitions into the state of quark-gluon plasma. In this quark-gluon plasma, the particles exhibit quasi-free behavior. If only the baryon density is increased but the temperature remains low, a so-called color superconductor is expected. In this state of matter, the color charge of the quarks can be transferred without loss, similar to the electric charge in a superconductor.

Chiral symmetry QCD refers to the properties of quarks when they are considered massless. In reality, however, this symmetry is disturbed by spontaneous symmetry breaking, which leads to the mass generation of hadrons. Within this diagram, the chiral phase transition marks the transition state between different phases of the strong interaction. At low temperatures and high baryon densities, the quarks and gluons are in a hadronic state in which the chiral symmetry is broken and the quarks have effective masses. During the transition from the hadronic to the QGP phase, the chiral phase transition takes place, in which the spontaneous symmetry breaking of the chiral symmetry is reversed and the quarks become virtually massless [16].

One of the tasks of the CBM detector is to measure multi-strange hyperons, charmed particles and vector mesons decaying into lepton pairs arising from nuclear reactions under these conditions within the FAIR energy range with unique precision and accurate statistics. In order to achieve the required precision, the measurements are carried out at Au + Au interaction rates of up to 10 MHz. This requires the implementation of extremely fast and radiation-hard detectors, an innovative concept for data acquisition, analysis that includes free-streaming front-end electronics, and a high-performance computer cluster for online event selection.

In this context, the implementation of SiPMs in the Ring-imaging Cherenkov detector (RICH) (described in more detail in subsection 2.2) is also discussed as a possible upgrade. The unique combination between an accelerator system generating a high-intensity beam of heavy ions and advanced high-rate detectors based on innovative detector and computer technology creates ideal conditions for a research program with significant potential to discover fundamental properties of QCD matter.

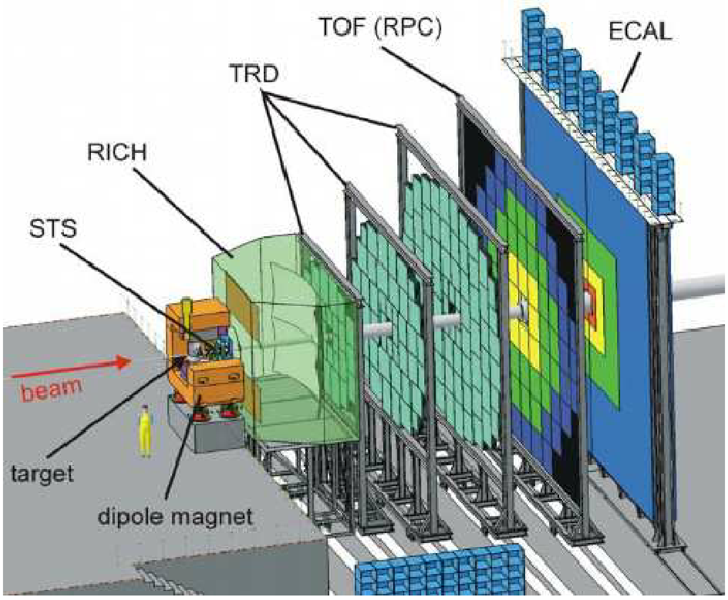

Figure 2: scetch of the CBM Experiment in its election configuration including the RICH detector for lepton ID [2].

Figure 2 shows the different subdetectors used in the CBM experiment. The Silicon Tracking System (STS) will be used to reconstruct the tracks of charged particles and determine their momentum. It consists of 8 tracking layers equipped with double-sided silicon microstrip sensors, arranged at a distance of 30 cm to 100 cm from the target and provides a momentum resolution of $\Delta p/p \approx 1\%$. The RICH detector is a focusing CO_2- gas RICH detector, which is used to discriminate pions from electrons. Its mode of operation is described in more detail in section 2.3. The Transition Radiation Detector (TRD) will be used for the discrimination of eletrons and pions with momenta in the range of GeV/c. The TRD is read out via rectangular pads which provide a resolution of 300 µm to 500 µm in width and 3 mm to 30 mm along the pad. Every second transition radiation layer is rotated by 90° for improving spatial resolution. With a pion suppression factor in the order of 100. The expected hit rate of the TRD will be 100 kHz/cm^2. The Time-of-Flight (TOF) detector, with an estimated area of around 120 m^2, is one of the largest detectors in the CBM experiment. Its primary purpose is to register the time of flight for β-determination between START-Detector and TOF. Its structure is based on Multigap Resistive Plate Chambers (MRPC), which consist mainly of resistive glass plates coated with conductive material, such as copper, on their outer surfaces. A gas filling is arranged between the plates. When a charged particle penetrates an MRPC (or the detector) it causes an ionization inside the Gas. Due to large electrical field gradient an avalanche amplification occurs and the resulting charge can be read out. The TOF detector achieves a system time resolution of less than 80 ps [17].

2.1 Cherenkov Radiation

In this section, the creation of Cherenkov photons is discussed in more detail to explain why this radiation can provide information about the velocity of charged particles. Cherenkov photons are emitted when the velocity of a charged particle $v = \beta c$ passing through a medium exceeds the phase velocity of the light in the medium. The emission of photons is caused by a brief polarization of the electron shells of the atoms, which results from the particle passing through. This polarization creates a time-varying dipole moment, which produces electromagnetic radiation. If the velocity of the particles passing through the medium is lower than the phase velocity of the light in this medium, the dipole moments can arrange themselves regularly, resulting in a total effective dipole moment of zero. If the speed of the particle exceeds the phase velocity, arranged dipole moments are formed (Figure 3). This leads to the total dipole moment no longer being zero and thus an emission of electromagnetic spherical waves at every point of the particle trajectory. A wave front that is emitted at a certain angle θ towards the direction of travelling of the particle gets initiated, the emission angle of the emission of which is dependent on its velocity. This is shown in Figure 4.

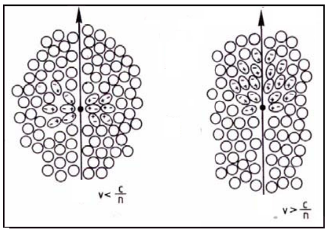

Figure 3: Resulting Dipoles of a charged particle passing through matter [12].

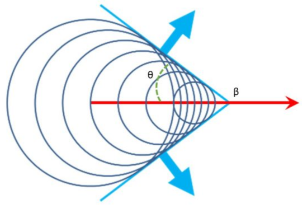

Figure 4: Display of the Cherenkov cone [13].

The wave front propagates with the phase velocity of the light in this medium. The angle θ between the direction of emission and the direction of propagation can be determined using,

$$\cos(\theta) = \frac{\frac{c}{n} \times \Delta t}{v \times \Delta t} = \frac{1}{n \times \beta} \tag{1}$$

with the Cherenkov angle θ, speed of light c, the refraction index n and the time window Δt. From this equation the conditions particles must fulfill to produce Cherenkov light can be estabished. Thus, a minimum velocity $v_{min} = c/n$ and from this a minimum energy E_{min} can be determined, which the particles must have in order to produce Cherenkov light. This can be calculated using,

$$E_{min} = \frac{m_0 c^2}{\sqrt{1 - \beta_{min}^2}} = m_0 c^2 \sqrt{\frac{n^2}{n^2 - 1}}, \tag{2}$$

where m_0 is the rest mass of the particle. The radiator medium used in the RICH detector of the CBM experiment is CO_2, which has a refractive index of 1.00044 at 0 °C [14]. This corresponds to a minimum particle velocity of $0.99956c$ and thus a minimum energy of 17 MeV [15] for Cherenkov light emission of electrons. Pions also emit Cherenkov radiation from a momentum of 4.55 GeV/c. However, the detected rings of these have a smaller radius, so they can be distinguished from the rings of the electrons.

2.2 Ring Imaging Cherenkov (RICH) detectors

In this section, functioning and application areas of Ring Imaging Cherenkov detectors will be discussed in more detail. Ring Imaging Cherenkov (RICH) detectors are used to discriminate electrons and pions and determine the velocity of charged particles by measuring the Cherenkov angle θ. By combining this measurement with the particle momentum measured by other detectors, the identification of the respective particle can then be achieved. The principle based on Cherenkov radiation is explained in more detail in section 2.1. The RICH detection is structured as follows: First, it consists of a radiator, for example a large, gas-filled chamber. In the case of the CBM-RICH, CO_2 is planned as the radiator gas. Several spherical mirrors with a radius of curvature R_M are arranged around the particle beam so that the interaction point in the target and thus the starting point of the particles are at a distance R from the mirrors. The mirrors are aligned accordingly to the respective photomultiplier cameras (in the case of the CBM-RICH, the use of two cameras is planned: one above and one below the particle beam). These are located on a ring with a radius of $R_D = R_M/2$. Since the Cherenkov radiation propagates radially from the beam and the individual beams or photon trajectories run parallel to each other, a small ring will be visible on one of the cameras for each particle if the alignment is correct. The radius of this ring depends on the opening angle of the Cherenkov cone and therefore on the particle velocity. The cameras must be in the focal plane of the mirrors to enable focusing. This principle is illustrated in Figure 5.

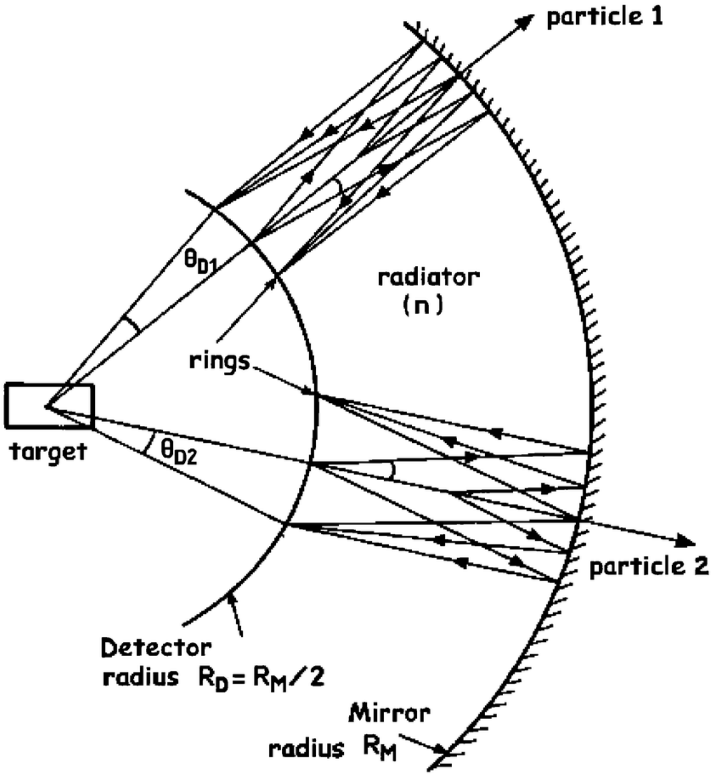

Figure 5: Sketch of the working principle of a RICH detector [23].

If a particle on a certain trajectory enters the radiator at a speed higher than the speed of light in the radiator medium, a Cherenkov cone is formed around the particle track. The spherical mirrors reflect this radiation and focuses it into a small circle that is imaged on the photo camera. Since this Cherenkov cone usually consists of only a few photons under experimental circumstances, the photocameras must be equipped with photomultipliers with which single photon detection is possible. Without the curvature, the Cherenkov cone would represent a circular area on the mirror. In order to obtain a usable result, it is not sufficient to measure the entire circular area, but this circular area must be reduced to a ring by the curvature of the mirrors, which is then recorded by the photocamera. The radius of these rings then depends solely on the speed of the particle that produced the Cherekov radiation. To determine the velocity of the particle, the radius of the circular ring produced by the Cherenkov cone on the mirror is first calculated

$$r = f_M \cdot \tan(\theta_c) = \frac{R_M \cdot \tan(\theta_c)}{2}. \tag{3}$$

Here f_M is the focal length of the mirror and θ_c is the Cherenkov angle. Using the small angle approximation $\tan(\theta) = \theta$ and $\theta = \arccos(1/\beta n)$, the equation can be solved for the velocity,

$$\beta = \frac{1}{n \cdot \cos\left(\frac{2 \cdot r}{R_M}\right)}. \tag{4}$$

If the momentum p of the particle is also known, the mass and particle identification can also be carried out [10],

$$p = m\gamma \cdot \beta c \Rightarrow m = \frac{p \cdot \sqrt{1-\beta^2}}{\beta c}. \tag{5}$$

2.3 RICH at CBM experiment

At the CBM experiment, the RICH detector is located directly behind the dipole magnet in which the Micro Vertex Detector (MVD) and the Silicon Tracking System (STS) are installed (Figure 2). The concept used is a gas RICH detector with a 1.7 m long CO_2 radiator volume at a relative over-pressure of 2 mbar. This gas offers good properties in terms of transmission behavior and an accurate refractive index. The refractive index is very important to distinguish eletrons from pions at these high pulses. It also has the advantage that it produces hardly any scintillation light. Other gases emit significantly more scintillation photons than Cherenkov photons, which would make detection of Cherenkov photons impossible. It is also advantageous for handling as it is neither highly flammable nor toxic and is affordable. For the detection of the Cherenkov photons, spherical mirror tiles are arranged in a mirror system. MAPMTs of the type H12700 from Hamamatsu are used, which may be replaced with SiPMs in the future. 80 trapezoidal plates with an area of 1600 cm^2 each, a radius of curvature of 3 m, and a thickness of 6 mm form the spherical system. It was manufactured from SIMAX glass with a Al+MgF_2 reflective and protective coating. These offer the advantage of good reflectivity for wavelengths up to 200 nm and a very homogeneous surface, which is important for ring sharpness. For each ring generated by an electron, 20-30 selected cherenkov photons are expected. Up to 100 rings are expected for each Au-Au collision with energies of < 8 GeV per nucleus. To measure particles from the rare dileptonic decays, the pions are suppressed with a suppression factor of 10^3 to 10^4. In addition, the detector structure allows for K mesons and pions to be separated from momentum above 5-6 GeV/c [10], [11].

3 SiPMs

This section deals with the theoretical foundation that is needed for understanding how SiPMs work. Therefore, its contains a description of the functionality and the structure of the SiPMs. In this section the characteristic parameters such as Dark Count Rate, crosstalk and gain that are investigated.

3.1 Structure of SiPMs

A SiPM is an array of avalanche Photo Diodes (APDs). Avalanche photodiodes use the photoelectric effect for charge carrier generation and the avalanche breakdown for internal amplification. They are mainly used for single photon detection at small wavelength [18]. The support material of SiPMs is a highly doped n-substrate, which is attached to an less n-doped avalanche zone. Then a matrix of highly doped p-layer is applied. Each element of this matrix represents a single microcell. To reach higher photon yields, each cell is coated with passivation layer to reduce the recombination rate on the surface. This passivation layer leads to a higher photon detection efficiency. The structure of a common SiPM is shown in Figure 6.

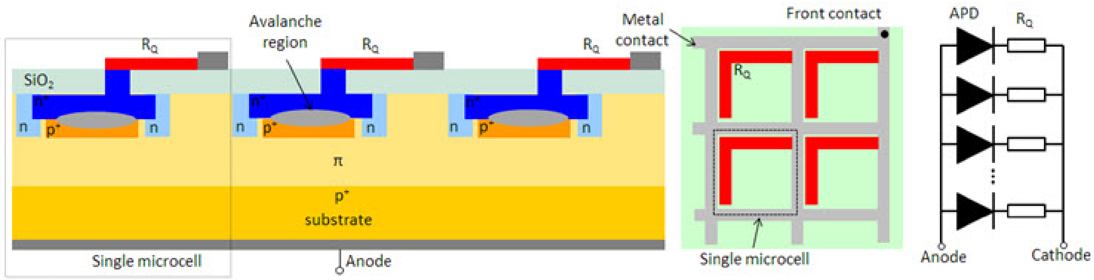

Figure 6: Typical structure of a SiPM [6].

Doping is the insertion of impurity atoms into a silicon lattice. If this is an n-doping, the inserted impurity atoms have more valence electrons than the carrier material. In the case of p-doping, the impurity atoms have fewer valence electrons. For silicon, this leads to doping with elements with 5 or 3 valence electrons. This process changes the electron density and creates quasi-free charge carriers on the doped atoms. However, doping does not change the neutral electrical charge of the material. The strength of the doping depends on the number of impurity atoms inserted. Pictures of p- and n-doped silicon crystals are shown in Figures 7 and 8. At a so-called p-n junction, where an n- and a p-doped layer meet, a concentration gradient of the charge carriers is created so that the electrons and defect electrons can recombine at this contact surface. This process creates an electric field due to the now charged doped atoms, which counteracts the concentration gradient until equilibrium is reached. A depletion zone without free charge carriers forms at the contact surface, which continues into the n-doped region [5].

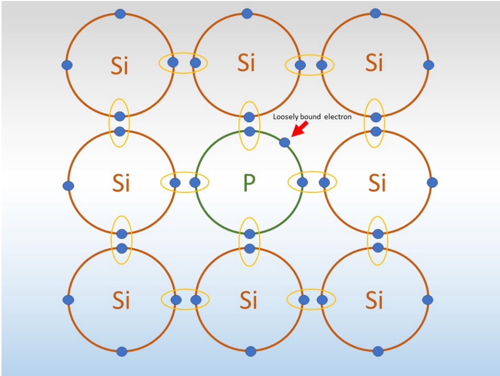

Figure 7: Sketch of an n-doped silicon crystal [7].

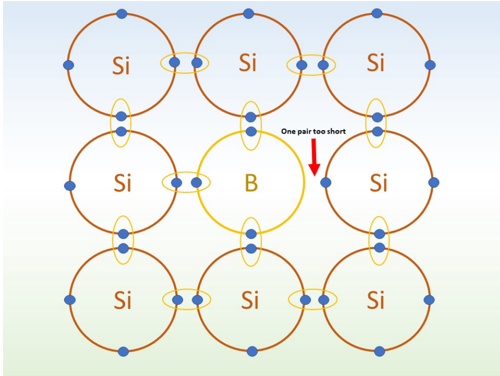

Figure 8: Sketch of an p-doped silicon crystal [7].

3.2 Functionality of SiPMs

The APDs are designed so that they can be operated above their breakdown voltage. These diodes are called Geiger Mode APDs (GM-APDs). Each cell of a SiPM is a combination of an GM-APD and a quenching resistor (RQ). All cells are connected in parallel. The equivalent circuit is shown in Figure 9. The equivalent circuit of an APD is shown in Figure 10.

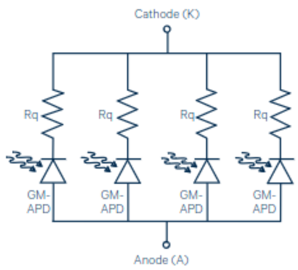

Figure 9: Parallel arangement of the different pixels of a SiPM with GM-APD in series with RQ [3].

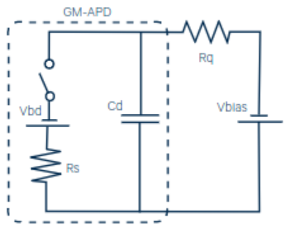

Figure 10: Sketch of the equivalent circuit of a GM-APD with series RQ and external bias containing a switch with models the turn-on and turn-off probabilities [3].

There are three basic operation modes of a GM-APD: quiescent phase, discharge phase and recovery phase. During the quiescent mode, the diode is reversed biased to $Vbias = Vbd + Vov$ (Vov is the over-voltage, i.e. the excess bias beyond the breakdown voltage Vbd). The switch in figure 10 is opened as long as no photon is absorbed and the diode will stay in this phase, with no current flowing. If a photon gets absorbed, or a dark count event happens, the imaginary switch closes and the Capacitor Cd discharges from $Vbias$ to Vbd through Rq. During this phase the avalanche breakdown inside the GM-APD is initiated. Avalanche breakdowns exhibit distinct mechanisms within the context of a PN junction. Within the depletion region of said junction, thermal energy plays a pivotal role in generating electron-hole pairs. The resultant leakage current arises from the migration of minority electrons, propelled by the electric field across the barrier region. Incremental elevation of the reverse voltage across the depletion region leads to a critical threshold being attained. Upon reaching this critical or breakdown voltage

Vbd, thermally released minority electrons acquire adequate energy to rupture covalent bonds upon collision with lattice atoms. The liberated electrons, further accelerated by the electric field, initiate a cascade effect, facilitating the release of additional electrons in a chain reaction [3] [4]. If this Process is started it is self sustaining, which means without any quenching, a steady current flows indefinitely in the device. This avalanche is also referred to as breakdown of the detector. This procedure is used for single photon detection. If a breakdown happens, the number of photoelectrons do not matter anymore, that is why the amplification Factor G, also referred to as gain is only proportional to the over-voltage and Cd,

$$G = \frac{Vov \times Cd}{e} \tag{6}$$

The gain represents the electrons that are produced by an incoming photon. It normally reaches a value of $G \approx 10^5 - 10^7$. The proposed gain values for the three SiPMs used can be looked up in Table 1. With Rq the avalanche breakdown process is quenched and the switch is reopened again. After that the GM-APD enters the recovery phase. In this phase Cd recharges back to $Vbias$ through Rq and the GM-APD returns to quiescent mode and is ready for the detection of a new photon [3]. The time that the SiPM is in the recharge phase is called dead time. The parallel connection of the different cells add currents of photons arriving at the same time and thus the peak heights correlate with the number of photons. These are subsequently referred to as n-photon equivalent (npe) [8]. In Figure 11 the accumulation of SiPM signals representing the npe peaks.

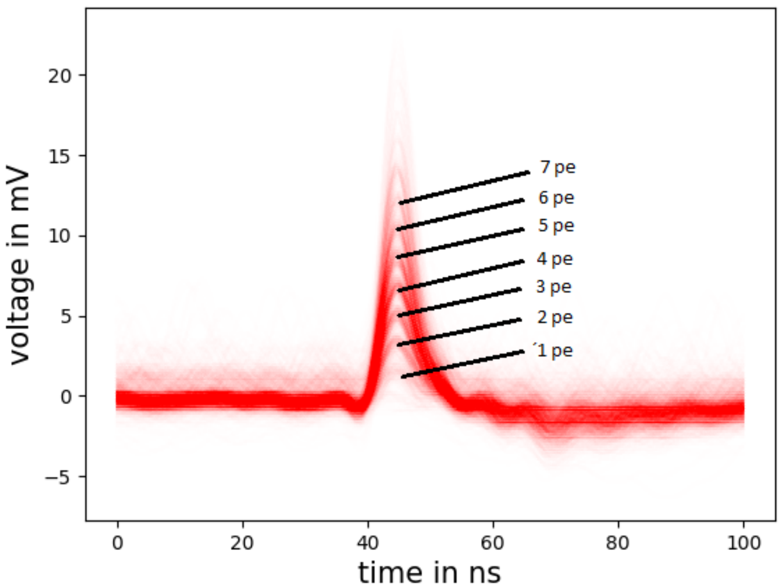

Figure 11: Accumulated signal traces which represent the npe peaks of the amplified signal for the Hamamatsu S14160-6050HS SiPM at 42 V bias voltage and 20 °C.

3.3 Dark count Rate

Due to the thermal agitation of electrons in the silicon crystal, it occasionally happens that a valence electron bound to an atom is lifted into the conduction band by thermal energy and is accelerated as a result of the electric field. This thermally excited electron can trigger an avalanche of electrons, similar to a photoelectron, and thus generate a signal that is indistinguishable from a photoelectron generated by light. This background noise is called the dark rate. The DCR for each of the three SiPMs are displayed in Table 1. SiPMs have a higher DCR ($\sim$ 10 MHz per pixel), which is a disadvantage compared to MAPMTs ($\sim$ 10-100 Hz per pixel). Due to the origin of DCR in thermal movement of the electron, the DCR is increasing significantly with temperature. Another influencing variable is the over-voltage Vov. The higher this voltage, the less the electrons are bound to the silicon lattice, making it easier for them to be released by thermal movement. However, by increasing the gain through an increase in Vov, a higher Vov is preferred. The effect of over-voltage on the DCR is reduced at lower temperatures and can be neglected at sufficiently low temperatures [8]. The DCR is determined by determining the single photon equivanlent spe and counting out all peaks above this value from a signal.

3.4 Crosstalk

When a cell triggers an avalanche, electrons can recombine with holes and generate photons in the near-infrared (NIR) range at ≈ 1100 nm. These photons can travel relatively long distances in silicon and generate electron-defect electron pairs in neighboring microcells, which in turn trigger avalanches. The secondary avalanches occur so shortly after the first that they are detected simultaneously. This process can also spread to other microcells, resulting in significantly higher signals above the noise level. The probability of crosstalk events is proportional to the gain factor or over-voltage (Vov). It is possible to reduce, but not completely eliminate, the crosstalk events by using photon-absorbing layers, called trenches, between the cells [8]. The crosstalk values specified by the manufacturer are given in Table 1.

3.5 Afterpulsing

In crystalline structures, such as those found in silicon photomultipliers (SiPMs), irregularities can occur in the form of lattice defects. These defects in the lattice can temporarily trap electrons during a charge pulse multiplication, also known as an avalanche. These electrons can later trigger an additional charge pulse multiplication, known as an afterpulse. The lifetime of an electron in a lattice defect varies depending on the type of defect and typically ranges from a few nanoseconds to a few microseconds. This lifetime is generally inversely proportional to temperature, as higher temperatures lead to increased movement of the particles and it is therefore more likely that electrons will be released from a lattice defect.The probability of an afterpulse depends on several factors. On the one hand, it increases with the number of existing lattice defects and on the other hand with Vov. An increased Vov leads to a higher probability of afterpulses, as it accelerates the electrons more strongly. Furthermore, the probability of an afterpulse depends on the charge already present on Cd. The height of the afterpulse peaks is therefore dependent on the charge of Cd. If an electron has already been released from the lattice defect before the voltage rises above Vbd, no afterpulse occurs. The probability of an afterpulse also increases if the amplification factor (gain) and thus the number of electrons is increased. This increases the chance of an electron hitting a lattice defect. The afterpulse probability specified by the manufacturer for the various SiPMs can be found in table 1 [8].

SiPM	**MICROFJ -60035**	**S14160 -6050CS**	**AFBR S4N66P024**
Vendor	OnSemi	Hamamatsu	Broadcom
Pixel pitch (μm)	35	50	40
Fill factor(%)	75	74	80
V. operating (V)	30	40	45
PDE (%)	50	50	63
Gain ($\times 10^6$)	6.3	2.5	7.3
DCR (kHz/mm^2)	150	100	125
Crosstalk (%)	25	7	23
Afterpulsing (%)	5	-	1

Table 1: Manufacturer information about the three inverstigated SiPMs

4 Experimental setup

This section describes the cooling system and the amplification system. The SiPM is installed in a container that is as light-tight as possible, which is subsequently referred to as a dark box. A cable for power supply and a cable for signal transmission, which is connected to a digital RTO1044 oscilloscope is lead out of the dark box. A precision voltage source AGILENT E3631A provides the bias voltage for the SiPM. The Laser is placed outside the Dark Box and it is controlled by the PLDD-20M Laser Diode Driver from ALPHALAS. The laser is controlled in such a way that it sends a 100 kHz signal of ultra short laser pulses of around 20 ps through an optical fiber to the SiPM. The laser diode driver also provides the trigger signal for the oscilloscope. The SiPM detects the light of the laser and generates an output signal. This SiPM signal is amplified via an amplification circuit, which is described in more detail in section 4.1, and passed on to the oscilloscope. The temperature of the SiPM is kept constant during the process via the control system, which is described in more detail in section 4.2. Figure 12 shows the setup of the experiment. Pictures of the three SiPMs used are shown in Figure 13.

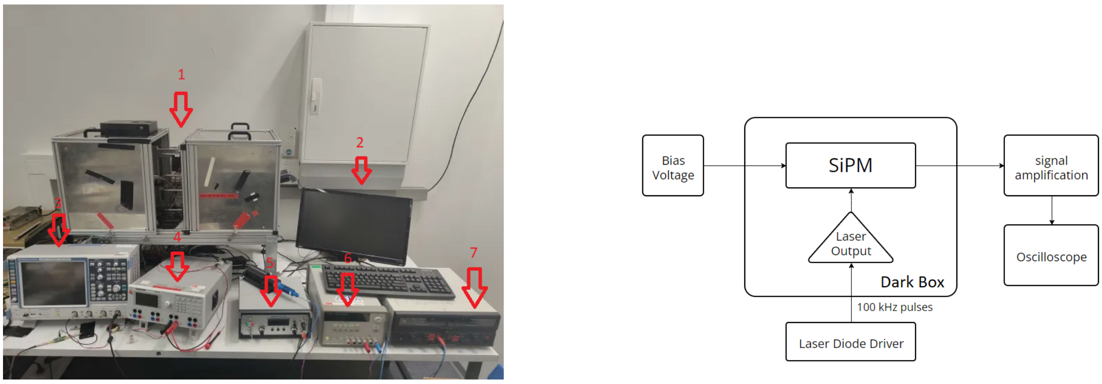

Figure 12: The setup of the experiment once as a schematic representation and once in the laboratory (1:Dark Box, 2:Raspberry Pi control, 3:Oscilloscope, 4:Amplification voltage supply, 5:Laser Diode Driver, 6:SiPM bias voltage supply, 7:Temperature control supply).

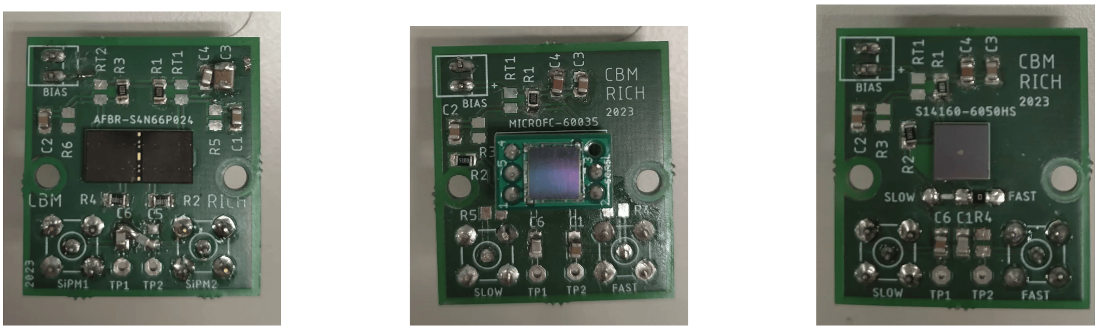

Figure 13: SiPMs used in the investigation (left: Broadcom AFBR S4N66P024M, middle: OnSemi MICROFC-60035, right: Hamamatsu S14160-6050HS).

4.1 Amplification circuit

A Class-A amplifier serves to amplify SiPM signals, favored for their versatility, simplicity, linearity and fidelity in preserving signals at high frequencies, thus finding application in low noise, low gain blocks in RF systems. The amplifier's schematic, depicted in Figure 14, illustrates its configuration.

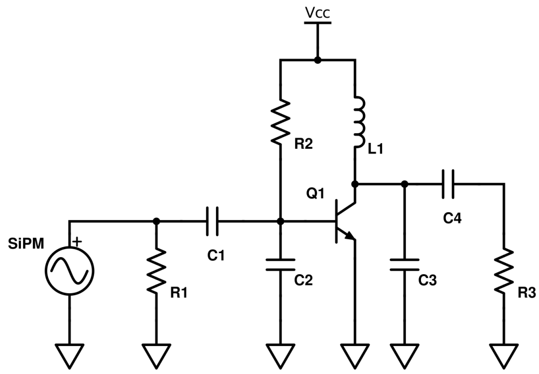

Figure 14: SiPM amplification circuit.

In this amplification circuit, R_1 ($50\,\Omega$) defines the input impedance, while C_1 (10 nF) acts to block the DC component of the input SiPM signal. Meanwhile, C_2 (1 pF) serves to stabilize the pulse baseline. R_2 ($10\,\mathrm{k}\Omega$), the bias resistor, regulates the amplifier working point and thus the collector current in transistor Q_1 (BFU760F) during its cut-off mode. Although current flows through inductor L_1 ($2\,\mu$H), no AC power is directed to the load resistor R_3 ($50\,\Omega$). However, during active mode, the transistor's collector current swiftly rises and falls, with the load dissipating AC power. Notably, the inductor stores energy during the transistor's cut-off mode, enhancing dynamic range. Capacitor C_4 (10 nF) serves to eliminate the DC component from the output signal, with all components within the amplification stage mandated to meet bandwidth requirements.
Operating on a 1.1 V power supply, the amplifier incorporates an LC low-pass filter in series with the bias voltage to mitigate high-frequency noise. Comprising a ferrite bead BLM15HG601SN1D and a capacitor bank ($10\,\mu$F, 100 nF, and 10 nF), this LC filter ensures signal integrity. The amplification board's design is depicted in Figure 15 [22].

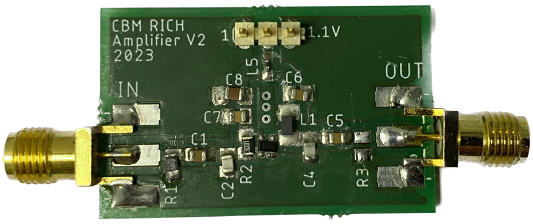

Figure 15: The amplification board. The bias terminal is connected to 1.1 V [22].

4.2 Temperature control system

The temperature control system is used to keep the temperature constant during the measurement. The SiPM is mounted on an aluminum plate and inserted into the dark box. To determine the temperature of the SiPM at a certain point in time, the temperature of the aluminum plate is measured via a DS18B20 sensor which is in contact with the plate and the SiPM. The sensor is connected to a Raspberry Pi. A python program is executed on this microcomputer on which a target temperature can be set. With the help of this program, the Raspberry Pi compares the SiPM temperature with the target temperature. Two Peltier cells are attached to the aluminum plate. The Peltier cells used here can heat and cool via the Peltier effect. Depending on the difference between the SiPM temperature and the target temperature, the Raspberry Pi adjusts the current applied to the Peltier cells via a power driver and can control the heat exchange between the cells and the aluminum plate. As the SiPM is directly connected to the aluminum plate, its temperature is also adjusted. Aluminum is used as the material here because it has good thermal conductivity properties so that the temperature difference between the plate and the SiPM is negligible. This provides constant cooling for the entire system consisting of Peltier cells, aluminum plate and SiPM. This system can also be used to cool the SiPM down to temperatures below room temperature. The advantage of the system is that the different temperatures can be set by changing a single parameter, the current applied to the Peltier cells. The system is first allowed to run until the environment temperature has been set as the actual temperature. The power source for the Peltier cells are then switched on and the system is left running until the actual and target temperatures differ by only 0.3 °C and then a measurement starts.

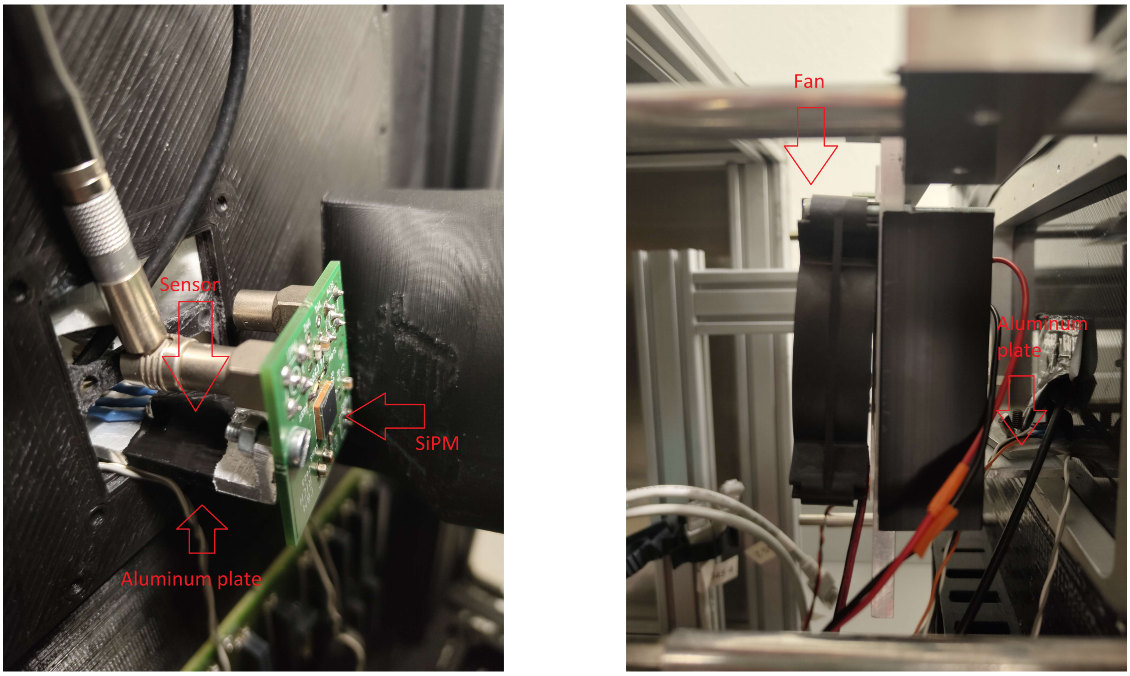

Figure 16: The setup of the temperature control in the laboratory.

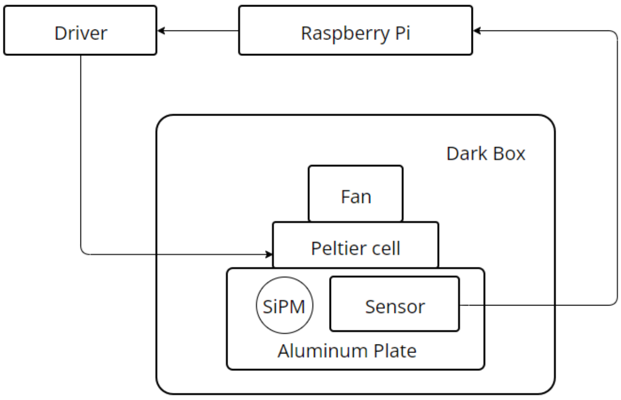

Figure 17: Schematic of the temperature control.

5 Analyzing procedure

In this section, the analysis process SiPM noise is described.

5.1 Determination of threshold values

In this section, the threshold values are determined. These are needed in further analyses to determine, whether the signal peaks have a voltage value that corresponds to the avalanche triggered by a single photon or by two different photons. After a temperature has been set and a bias voltage has been applied to the SiPM, 2000 pulses are recorded for a time window of 100 ns with a time resolution of 10^{-10}s. Figure 11 is obtained from the superposition of the 2000 pulses. First, the maximum value within the time window is determined for each pulse. All these maximum values are then plotted in a histogram against the voltage. These histogram peaks are fit by means of Gaussian distribution functions to derive center value and width,

$$f(x) = \frac{1}{\sigma\sqrt{2\pi}} e^{-\frac{1}{2}\left(\frac{x-\mu}{\sigma}\right)^2} \tag{7}$$

with the mean value μ and the standart deviation σ. The mean value of every Gaussian fit is then used to determine the difference between consecutive histogram peaks. An average value is then determined from these differences. This mean value, called single photon equivalent (spe) is multiplied by 0.5 to determine a threshold value above which signals must lie in order to be evaluated as a single photon event. This value is referred to as single photon threshold (spt). To determine a value above which signals must lie to be counted as a double photon event, the spe is multiplied by 1.5. This value is referred to below as the double photon threshold (dpt). The histogram that follows, including the fits and the resulting threshold values, can be seen in Figure 18.

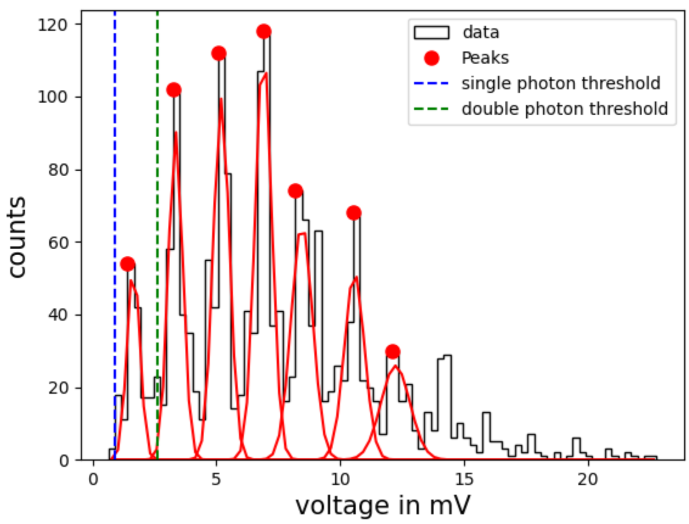

Figure 18: Amplitude spectum of the amplified signal for the Hamamatsu S14160-6050HS SiPM at 42 V bias voltage and 20 °C.

The gain of a SiPM is proportional to the spe values. The approximation,

$$\text{gain} \sim \frac{spe \cdot \sigma \Delta t}{2ARe} \tag{8}$$

is used [21] to calculate the gain values. Here Δt corresponds to the pulse width at the base line, which in this case is 10×10^{-9}s. σ is the pulse shortening ratio, which in this case is 14.4. R is the load resistance, which in this case is $50\,\Omega$. A is the amplification factor, which is 17.6 and e is the electron charge. This approximation is possible because the spe reflects the amplitude of a peak that mirrors the generated voltage of a charge avalanche triggered by a single photon. This equation can therefore be used to determine the number of electrons produced by an incoming photon, which is referred to as gain in 3.1.

5.2 Examination of the noise data

Data is recorded to determine the dark count rate, crosstalk and afterpulsing. For this purpose, The SiPM is kept under same conditions and temperature as for the the determination of crosstalk. Now, however, 2000 laser pulses are recorded for a time window of 2000 ns with a resolution of 10^{-9}s per sample. The time window was chosen, so that the recorded data for each pulse consists mostly of noise. The laser pulse has a width of $10 \cdot 10^{-9}$s and thus accounts for only 0.5% of the total recorded signal. Thus, the noise can be analyzed with this data. If one now plots all 2000 traces superimposed to each other, one gets a graph like the one in Figure 19.

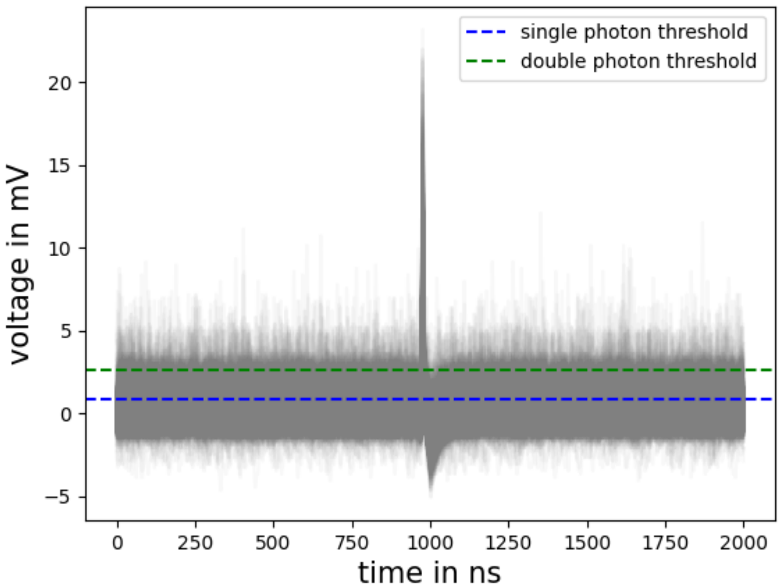

Figure 19: Amplified Signal for noise determination for the Hamamatsu S14160-6050HS SiPM at 42 V bias voltage and 20 °C.

The data set for each SiPM signal therefore contains 2000 data points due to the sample rate. First, peaks are searched for in these 2000 data points. A peak is a data point that has a higher voltage value than the data point of the previous and following sample. It is then determined for each peak whether is above the spt or dpt threshold. This procedure is carried out for all 2000 data sets. Figure 20 shows the determination of the peaks for a single pulse.

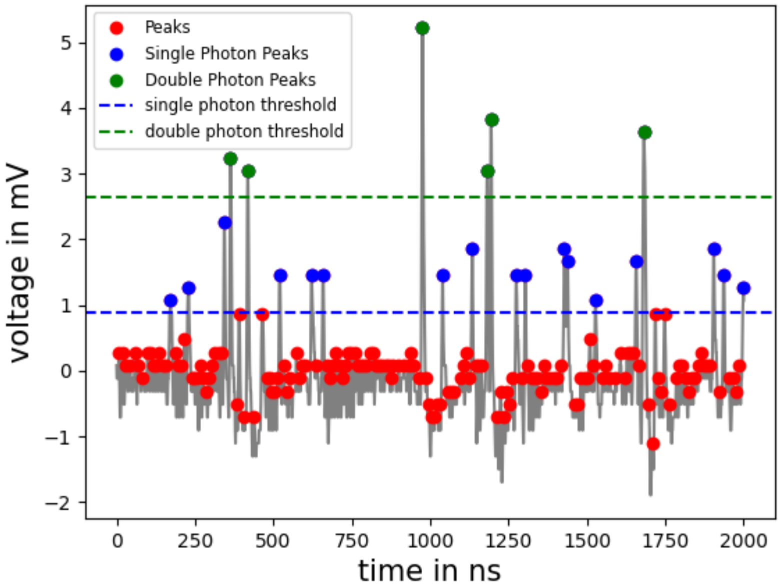

Figure 20: Example for peak determination for one puls for the Hamamatsu S14160-6050HS SiPM at 42 V bias voltage and 20 °C.

5.2.1 Determination of SiPM dark count rate

As described in section 3.3, dark count rate results from avalanches that are not triggered by photons, in the area outside the laser pulse. The laser pulse is visible as a peak in Figure 19. Peaks in the signal that lie above the previously determined spt are searched for. The DCR value is then determined using the following formula,

$$\mathrm{DCR} = \frac{\text{number of peaks above spt}}{N \times K \times 10^{-9}\mathrm{s} \times 36\,\mathrm{mm}^2} \tag{9}$$

with the number of samples K number of pulses N and the active area of the SiPM of $36\,\mathrm{mm}^2$, which is the same for every SiPM used. The DCR measured in $\mathrm{Hz/mm}^2$ is obtained from this calculation.

5.2.2 Determination of SiPM crosstalk

Since crosstalk describes events in which a photon triggers two charge avalanches in two different microcells and thus generates a signal that is equivalent to one that was triggered by two different photons (section 3.4). In order to determine the crosstalk probability, all peaks in the dark signal that lie above the double photon threshold (dpt) are first determined. Then, the following ratio is calculated,

$$P_{\text{crosstalk}} = \frac{\text{number of peaks above dpt}}{\text{number of peaks above spt}} \cdot 100 \tag{10}$$

to obtain a percentage value.

5.2.3 Determination of SiPM afterpulsing

Afterpulsing is also determined using the same signal. As described in section 3.5, the afterpulsing is triggered by electrons trapped in altered potentials of lattice defects, which are released after a certain period of time and then trigger another charge avalanche equivalent to one triggered by a single photon. Thus, to determine the afterpulsing, the number of peaks above the spt threshold in areas before and after the laser pulse with same width is compared. Figure 21 shows the ranges used. The following equation is used to determine the probability of afterpulsing as a percentage [20]:

$$P_{\text{afterpulse}} = \frac{\text{peaks above spt after laser pulse - peaks above spt before laser pulse}}{N} \cdot 100 \tag{11}$$

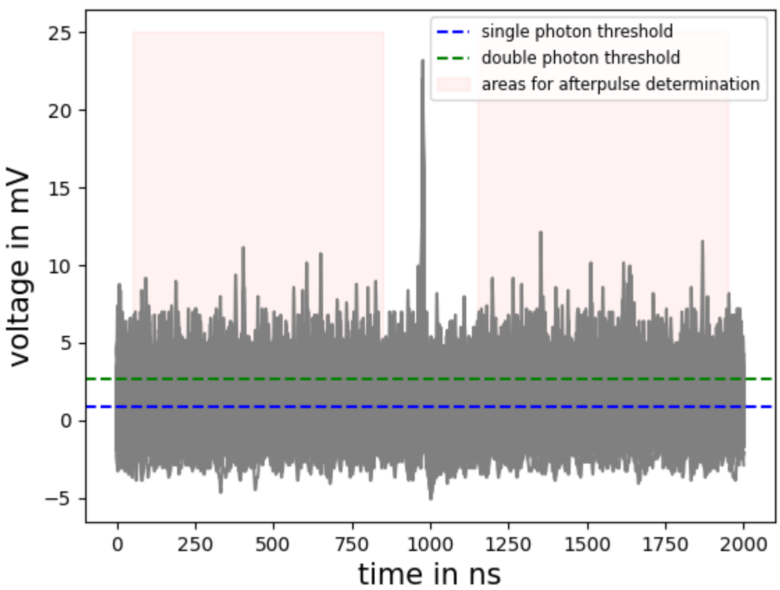

Figure 21: Ranges for afterpulse determination of the amplified signal e.g. Hamamatsu S14160-6050HS SiPM at 42 V bias voltage and 20 °C.

With this method, the difference in the number of peaks above the spt before and after the laser pulse is first determined for each individual pulse. It is now expected that this difference is positive, as more pulses occur after the laser pulse than before it due to afterpulsing. It then indicates the number of afterpulses measured. If this procedure is repeated for all 2000 pulses and the mean value of all differences is then divided by the number of measurements N carried out, the probability that an afterpulse occurs in the area after the laser pulse is obtained.

5.3 Afterpulse analysis

An analysis of the values using the method described above led to unexpected results, which is why a further analysis was carried out regarding the accuracy of the analysis method for afterpulsing. For this purpose, 2000 pulses were taken with the Hamamatsu S14160-6050HS SiPM and the difference between the number of the peaks over the spt before and after the laser pulse was determined for each individual pulse as in the method described above. These differences are then plotted in a histogram in figure 22.

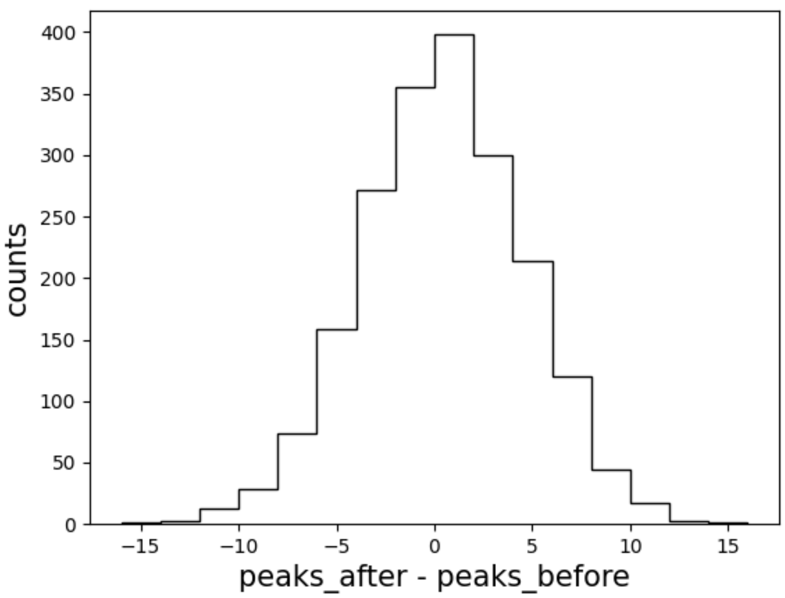

Figure 22: Distribution of peak differences for afterpulse determination e.g. Hamamatsu S14160-6050HS SiPM at 42 V bias voltage and 20 °C.

The mean value and the standard deviation of this distribution are then determined. It is sufficient to multiply the mean value by 100 in order to obtain an afterpulse probability. The standard deviation of the distribution is also multiplied by 100 to obtain the standard deviation of the afterpulse probability. Now the statistical error is calculated according to err $= \sigma/\sqrt{N}$ is determined. The average afterpulse probability for 2000 pulses is -3.7 % with a statistical uncertainty of 9.2 %. From this it can be concluded that the afterpulse cannot be determined because the deviation in relation to the actual value is too large.

This can be attributed to the fact that the dark count rates and their fluctuations are very large in comparison to the afterpulse probability, and negative values occur. Due to this high error, afterpulsing is not taken into account in subsequent analyses. In further measurements, which are not carried out as part of this bachelor thesis, the number of recorded pulses could be significantly increased in order to reduce the statistical error and a shift in the position of the laser pulse could be taken into account.

5.4 Systematic test for reproducibility of the obtained results

For this purpose the variation of results obtained during repeated measurements under same conditions are used to estimate the systematic uncertainty of the obtained measurement results. A fixed temperature of 25 °C and a fixed bias voltage of 42 V are set and several comparison measurements are carried out. The data is taken with the Hamamatsu S14160-6050HS SiPM, but the results can be used for all used SiPMs as these are deviations in the values that do not depend specifically on the SiPM. All components are switched off and restarted once. Then the cable connections of the SiPM are disconnected and reconnected. In addition, the system is heated up once to 35 °C and cooled down again to 25 °C. Furthermore, a measurement is carried out at the same temperature and bias voltage on another day. After each of these actions on the system, a measurement is started and gain, DCR, crosstalk and afterpulsing are determined as described in section 5.2. All values are then plotted as shown in figure 23. To determine the error, the mean value of all measurements and the standard deviation is calculated. For the DCR error the standard derivation is divided by the mean value to get an relative error in %.

To determine the error for crosstalk and gain, the difference between the mean value and the maximum value of the 4 measurements is determined and this is used as the upper error limit and the difference to the minimum value as the lower error limit. This method is used because larger dark count rates (DCR) lead to larger errors. The difference between the DCR values concerning different temperatures and between the different SiPMs are greater than for gain or crosstalk. The upper error limit of the gain is 0.017×10^6 and the lower error limit is 0.014×10^6, The error limits for crosstalk are 1.385 % and 1.503 % and the relative error for DCR is 6.99 %. The error values for crosstalk refer to an absolute percentage value and do not represent relative errors. The errors are used for all DCR, crosstalk and gain values determined under these measurement conditions. This can be done because those are greater than the standard error of the arithmetic mean of the values for each pulse, which is determined via $\sigma(\mu) = \sigma/\sqrt{n}$ [19]. This error is <1% for all noise types and the gain. This means that only the systematic standard error is considered in the uncertainty calculation.

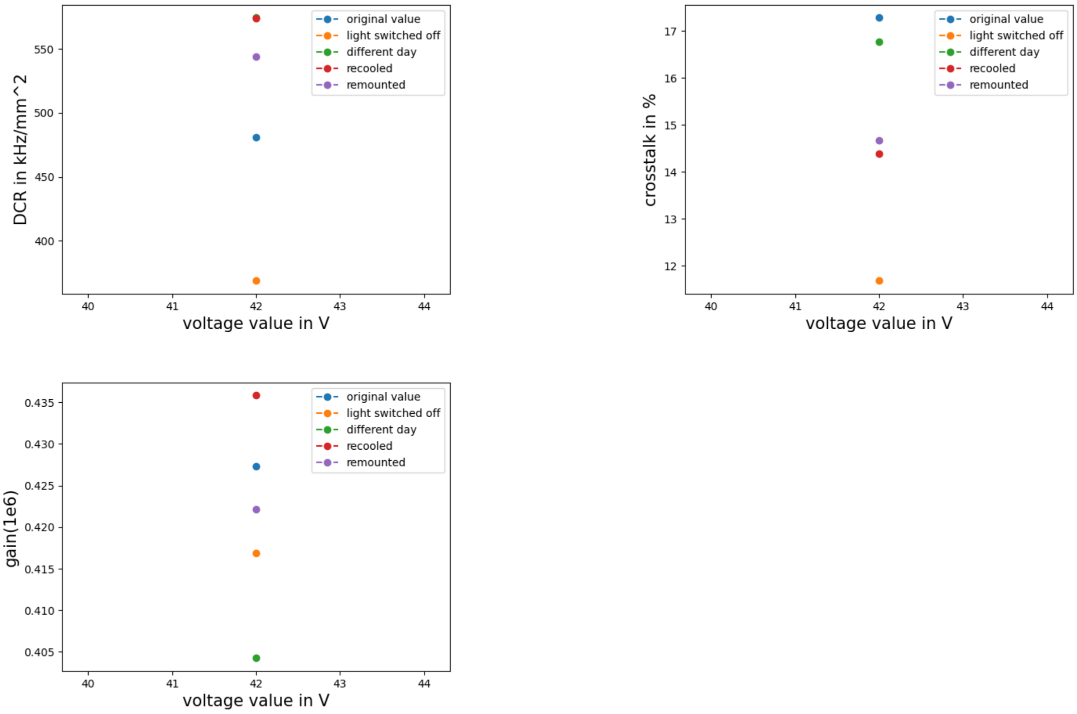

Figure 23: Plots for the error determination of the setup with light pollution.

In plot 23, a data point is also visible which is labeled "light switched off". This point shows a clear deviation from the other data points in terms of crosstalk and DCR. The light in the room was switched off prior to this measurement. The significantly lower values suggest that the dark box of the measurement setup in which the SiPM is located is not completely light-tight. As a result, light was entering the dark box and causing light pollution. DCR and crosstalk values are significantly influenced by the light pollution, as signals resulting from photons of external light are also incorrectly interpreted as DCR or crosstalk signals. However, the light pollution had no major effect on the gain values of the SiPM, as these have no effect as this indicates how many electrons are produced per incoming photon and here the number of incoming photons has no influence on this amplification factor. This also follows from the fact that the gain is determined via spe peak as in section 5.1 with external light pollution, the spe peak is still at the same point, the separation between the individual pe (figure 11) is just less clear. As the deviation can be attributed to the incidence of light, these values are not taken into account in the error analysis methodology described above. For this reason, the measurement setup was improved again and the dark box was sealed where possible and the light in the room was always switched off for the measurements. With the new measurement setup, new measurements are carried out to ensure the reproducibility of the results, which can be seen in Figure 24.

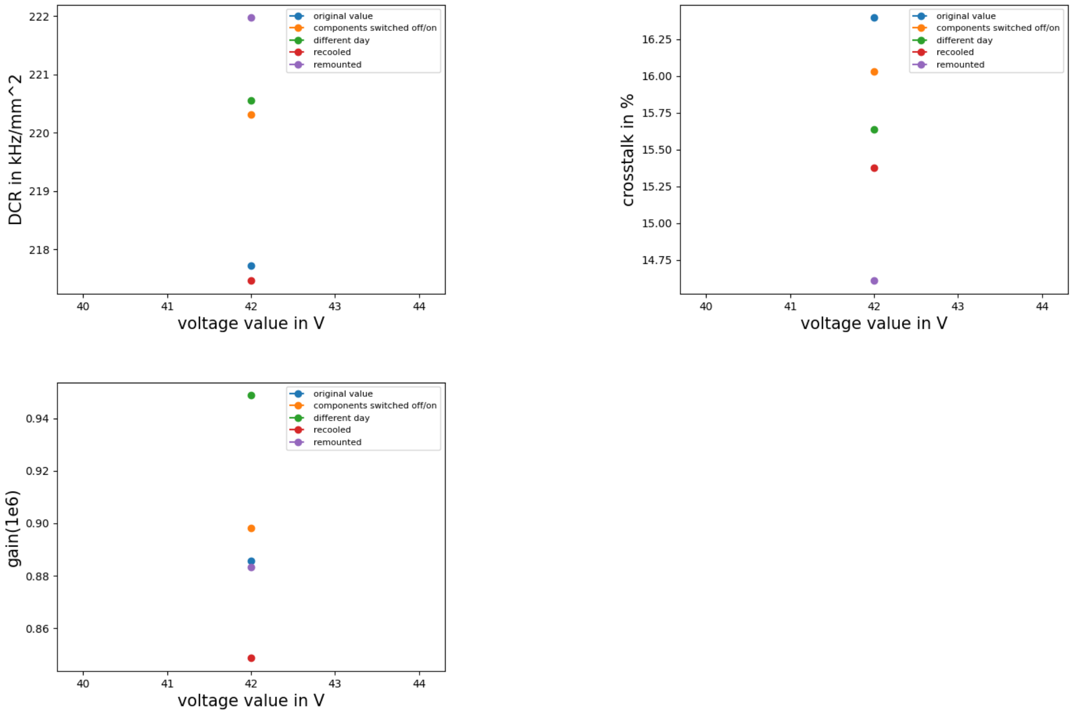

Figure 24: Plots for the error determination of the new setup.

For this measurements, a fixed temperature of 20.5 °C and a fixed bias voltage of 42 V is set for the same SiPM as the old setup. To do this systematic test, all components are switched off and restarted once, the cable connections of the SiPM are disconnected and reconnected, the system is heated up once to 35 °C and cooled down again to 20.5 °C and a measurement is carried out at the same temperature and bias voltage on another day. The same analysis is then carried out to determine the errors as before. For DCR values with the new setup, this now results in a relative error of 0.7 % . For the crosstalk values this results in an absolute deviation of 1 % upwards and 0.786 % downwards and for the gain of 0.044×10^6 upwards 0.055×10^6. The fact that the error is now significantly lower can be attributed to the new measurement setup, as there are now fewer fluctuations in the light intensity that were caused in advance by the external light irradiation, but still greater than the statistical error.

6 Results of DCR, crosstalk and afterpulsing analysis

The results are now presented in this section. The method described in section 5 was used to analyze for DCR, crosstalk and gain for temperatures ranging from 15 °C to 40 °C for all three SiPMs investigated. The bias voltages were also varied. However, the operating ranges for the voltage differed between the SiPMs. The operating range for the Broadcom AFBRS4N66P024 is 40 V to 46 V, for the OnSemi MICROFC-60035 it is 30 V to 34 V and for the S14160-5060CS it is 41 V to 46 V. These are the operating ranges for the SiPMs for which the signal was sufficiently clear, but not too noisy, to be able to perform an analysis. The noise values obtained are then plotted against the temperature and the applied bias voltage.

6.1 Temperature dependency

In the next step, the dependence of the DCR, crosstalk and gain values on the temperature is analyzed. Different temperature and bias voltage values are set, the data is recorded and the DCR, crosstalk and gain values are determined and then plotted. For some temperature and voltage values, it was not possible to obtain meaningful results from the signal using the analysis method, these do not appear in the following comparison graphs. For this analysis, data is used that was recorded with a setup that was not completely light-tight, as discussed in section 5.4. This leads to increased values in crosstalk and DCR. Outliers that occur are attributed to a change in the intensity of the light pollution resulting from a darkbox that is not completely closed, which increases the light irradiation. These data can nevertheless be used to make a statement about the temperature dependence, as light pollution is assumed that does not vary greatly between the different measurements. Although the values are therefore higher than expected, the dependency that is being investigated is nevertheless retained.

6.1.1 Comparison of DCR dependence on temperature

The DCR dependence on the temperature is considered. This dependence for the Broadcom AFBR-S4N66P024M SiPM is shown in Figure 25, for the OnSemi MICROFC-60035 in Figure 26 and the Hamamatsu S14160-6050HS in Figure 27.

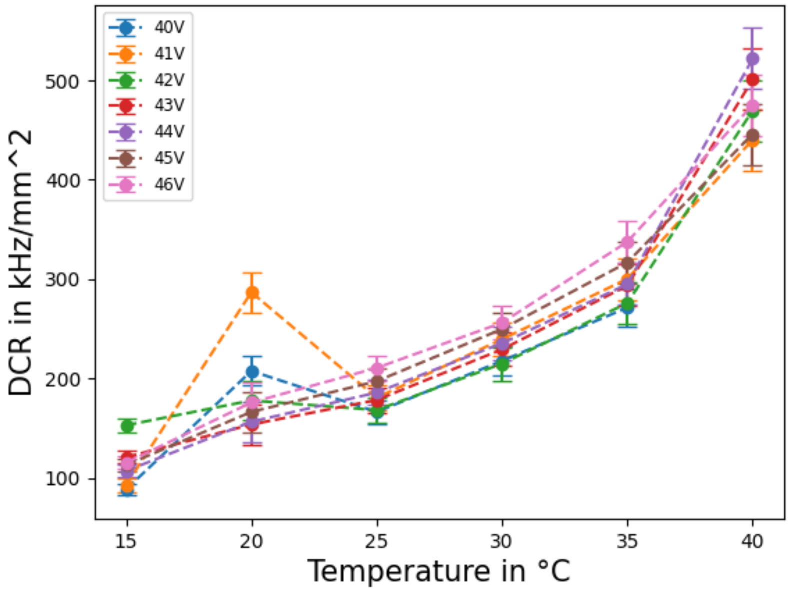

Figure 25: DCR plotted against temperature for Broadcom AFBR-S4N66P024M SiPM.

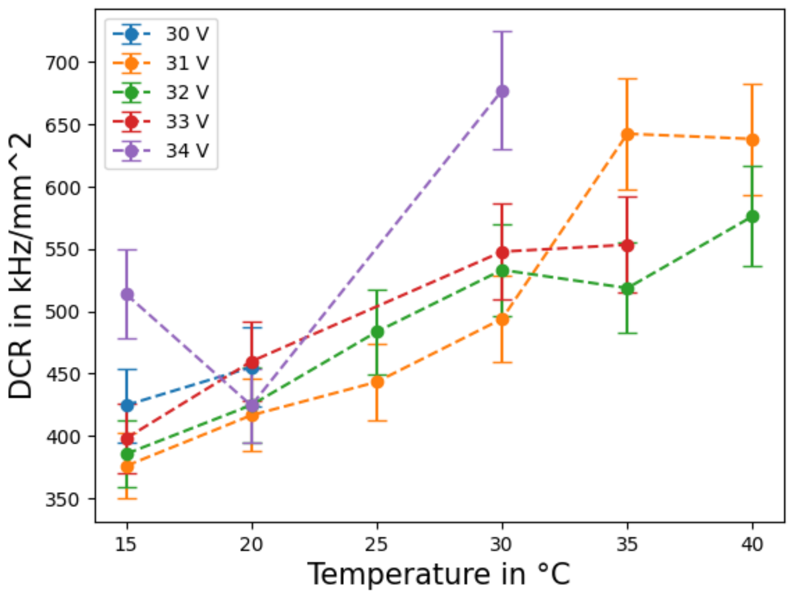

Figure 26: DCR plotted against Temperature for OnSemi MICROFC-60035 SiPM.

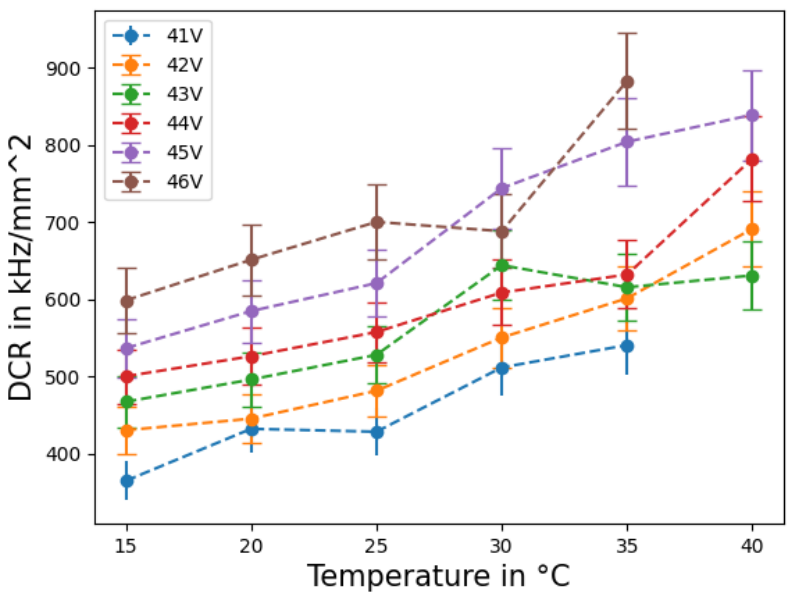

Figure 27: DCR plotted against Temperature for Hamamatsu S14160-6050HS SiPM.

An increase in DCR with increasing temperature can be seen at all three SiPMs. This is also expected, taking into account the main reason for DCR, as described in section 3.3 is the thermal agitation of the electrons. This gets faster with increasing temperature and explains the increase in DCR with temperature. In the Broadcom AFBR-S4N66P024M SiPM, two outliers are visible at 20 °C and 40 V as well as at 20 °C and 41 V. Two outliers are also visible at 20 °C and 34 V as well as 35 °C and 31 V for the OnSemi SiPM and Two are also visible for the Hamamatsu SiPM at 30 °C and 46 V as well as 30 °C and 43 V. A comparison of the increase in DCR with temperature under the different SiPMs shows that while the increase is almost linear for the OnSemi and Hamamatsu SiPMs, the Broadcom SiPM increases more strongly with increasing temperature. This is attributed to manufacturing variability, design differences and material differences between the various manufacturers.

6.1.2 Comparison of crosstalk dependence on temperature

The dependence of the crosstalk on the temperature is now considered. The uncertainties are the same for all values under consideration and this absolute error has been determined in section 5.4 and is not mentioned further here. The dependence of the crosstalk probability on the temperature of the Broadcom AFBR-S4N66P024M SiPM is shown in Figure 28 for the OnSemi MICROFC-60035 in Figure 29, and the Hamamatsu S14160-6050HS in Figure 30.

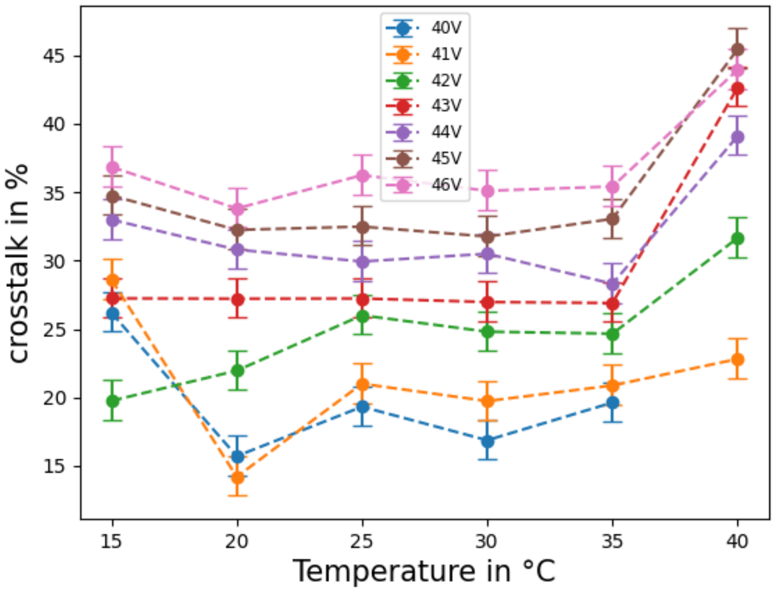

Figure 28: Crosstalk probability plotted against Temperature for Broadcom AFBR-S4N66P024M SiPM.

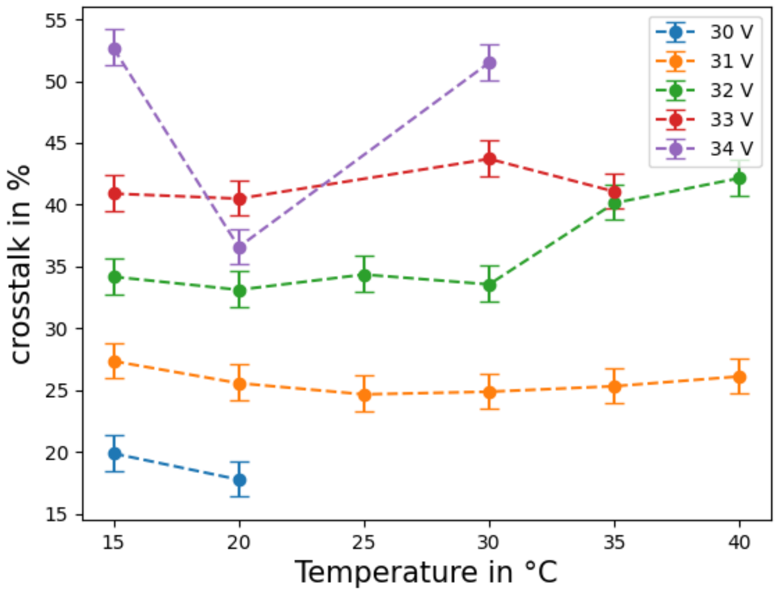

Figure 29: Crosstalk probability plotted against Temperature for OnSemi MICROFC-60035 SiPM.

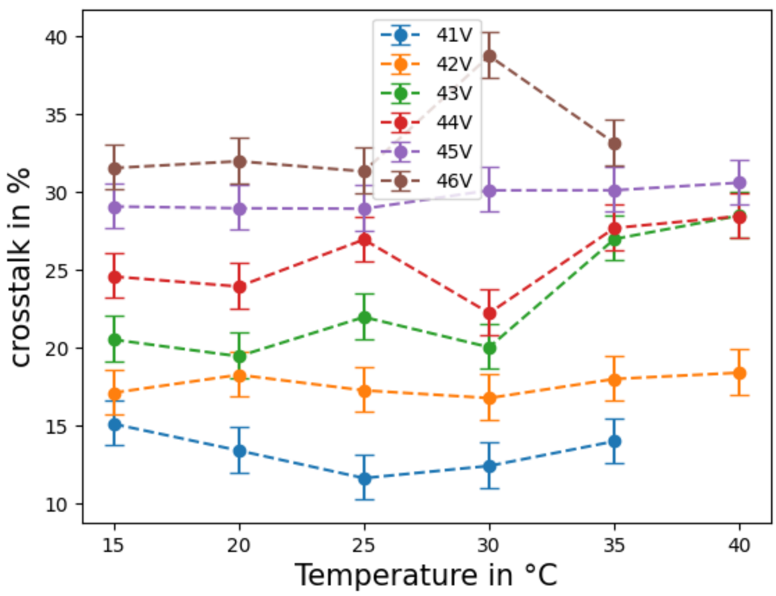

Figure 30: Crosstalk probability plotted against Temperature for Hamamatsu S14160-6050HS SiPM.

It can be seen that the crosstalk values remain almost constant with increasing temperature for each bias voltage for all three SiPMs. However for the Broadcom SiPM, it is also the case that the values for all bias voltages at 40 °C are higher than this previously almost constant value. These are also explained by an incompletely closed darkbox during the measurements at 40 °C and are therefore classified as outliers. In the context of these measurements it is assumed that the crosstalk values do not increase significantly in the temperature range under consideration and that they remain constant with increasing temperature. This is also the case for the small increase in the crosstalk values that can be recognized at 35 °C and 40 °C for the OnSemi SiPM. Outliers can also be seen at 15 °C and 40 V as well as at 15 °C and 41 V for the Broadcom SiPM, at 20 °C and 34 V for the OnSemi SiPM and at 30 °C and 46 V as well as 30 °C and 44 V for the Hamamatsu SiPM. In summary, the crosstalk probability for all three SiPMs remains approximately constant with increasing temperature at any voltage, if one do not consider the outliers. This can be explained by the fact that the crosstalk probability of a SiPM is determined by the intrinsic properties of the detector and its geometry, but not by thermal effects.

6.1.3 Comparison of gain dependence on temperature

The dependence of the gain on the temperature is now considered. As with crosstalk, the uncertainties are the same for all values considered, and this absolute error was determined in section 5.4. The dependence of the gain on the temperature of the Broadcom AFBR-S4N66P024M SiPM is shown in Figure 31 for the OnSemi MICROFC-60035 in Figure 32, and the Hamamatsu S14160-6050HS in Figure 33.

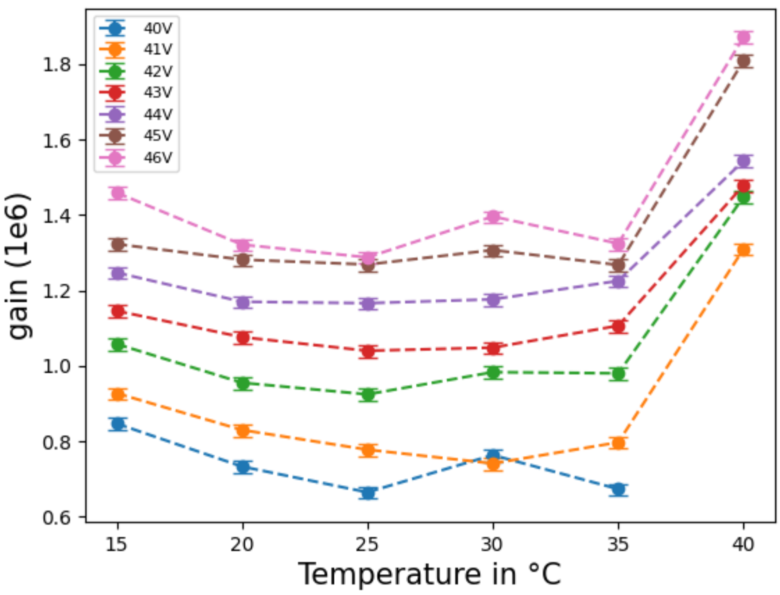

Figure 31: Gain plotted against temperature for Broadcom AFBR-S4N66P024M SiPM.

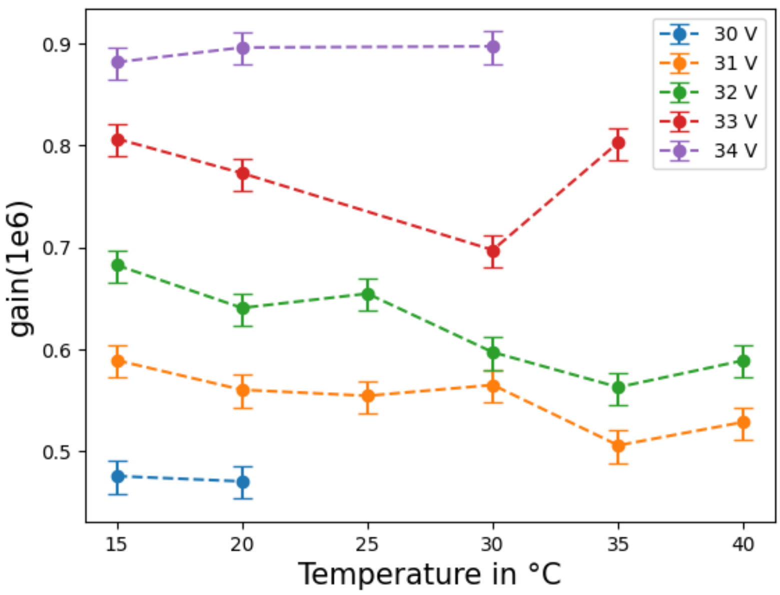

Figure 32: Gain plotted against temperature for OnSemi MICROFC-60035 SiPM.

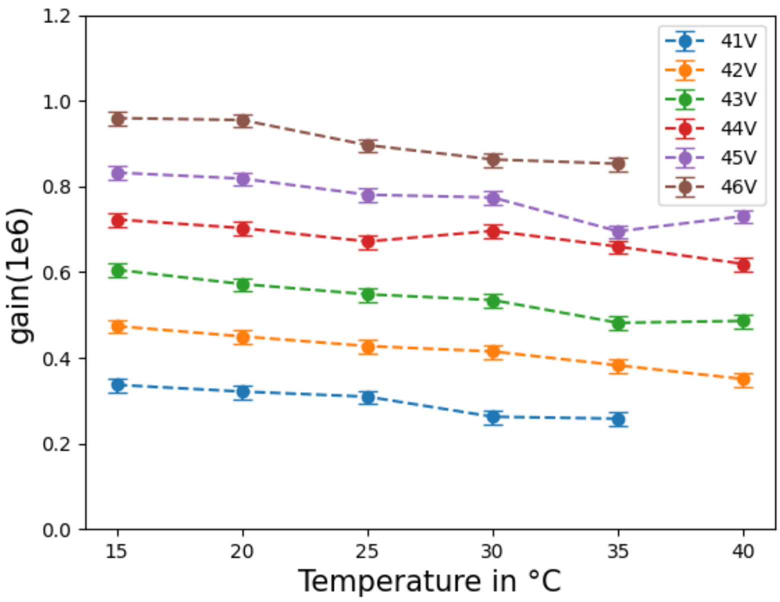

Figure 33: Gain plotted against temperature for Hamamatsu S14160-6050HS SiPM.

The gain values also remain almost constant for each operating voltage with increasing temperature for the Broadcom SiPM. This also shows a deviation from this constant behavior for gain at 40 °C. Which are classified as outliers for the same reasons mentioned in section 6.1.2 and are therefore not considered significant when examining the temperature dependency. The OnSemi SiPM and the Hamamatsu show a slight drop in the gain values with increasing temperature. This difference in behaviour is attributed to the different specific design of the SiPM with regard to gain stabilization functions, depending on the manufacturer. With the exception of one gain value at 30 °C and 40 V for the Broadcom SiPM there are no outliers visible.

6.2 Voltage dependency

The following section discusses the dependence of the DCR, the crosstalk and the gain on the bias voltage applied to the SiPM. All measurements were carried out at a fixed temperature of 20.5 °C. These measurements were carried out with the improved light density setup already discussed in section 5.4. With the help of this setup, more precise statements can be made about the noise behavior of the SiPM, since the light pollution is significantly lower. Therefore, in addition to the voltage dependence, the absolute values of the DCR of the crosstalk and the gain are also compared in this section in order to be able to make a recommendation. Figures on the voltage dependencies of the values recorded with the set-up used in section 6.1 can be viewed in section 8.

6.2.1 Comparison of DCR dependence on bias voltage

First, the dependency of the DCR on the applied bias voltage is examined in more detail. The plot for the Broadcom AFBR-S4N66P024M SiPM is shown in Figure 34 for the OnSemi MICROFC-60035 in Figure 35 and the Hamamatsu S14160-6050HS in Figure 36.

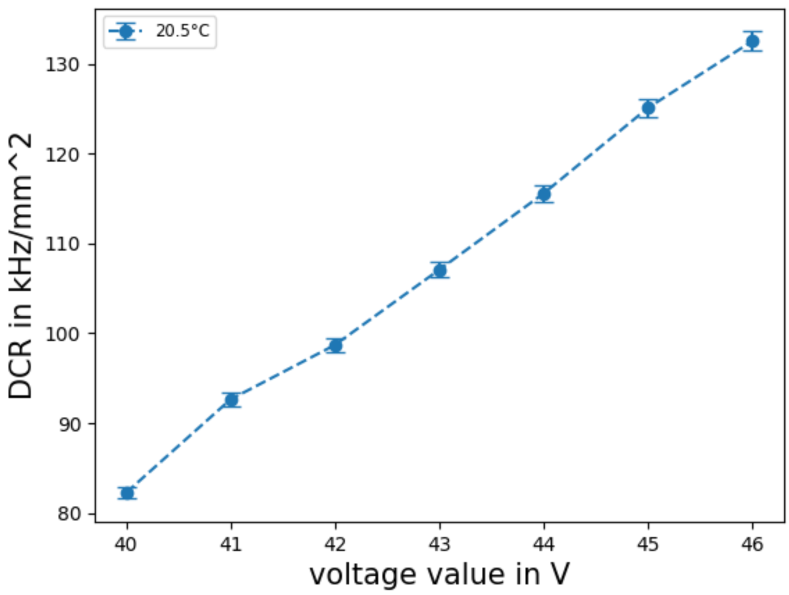

Figure 34: DCR plotted against voltage for Broadcom AFBR-S4N66P024M SiPM.

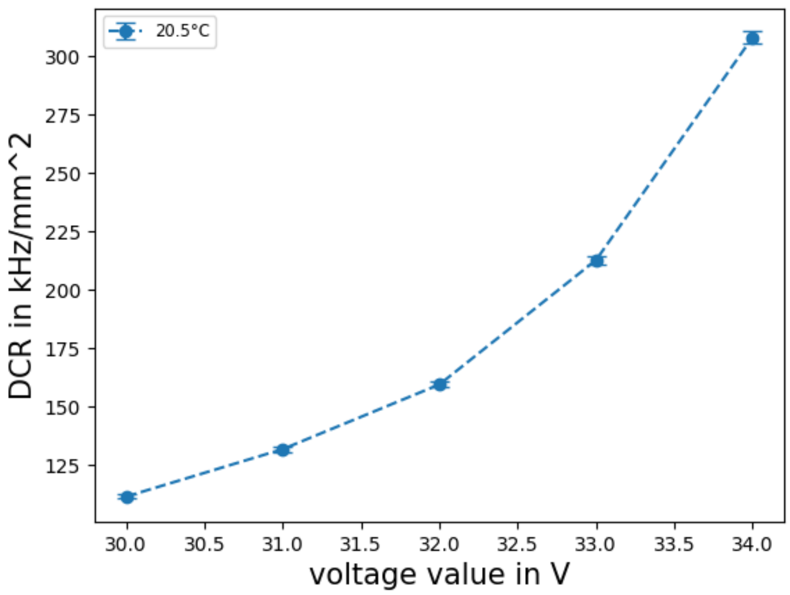

Figure 35: DCR plotted against voltage for OnSemi MICROFC-60035 SiPM.

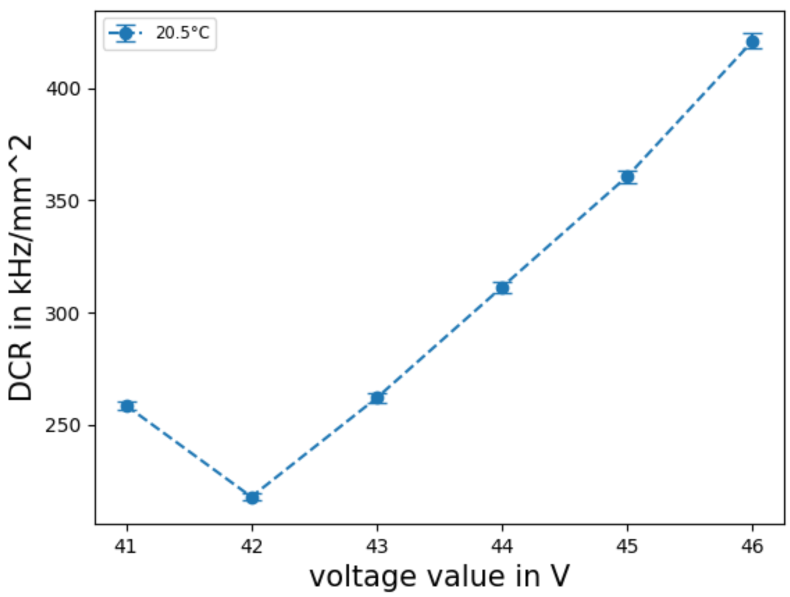

Figure 36: DCR plotted against voltage for Hamamatsu S14160-6050HS SiPM.

All three SiPMs show a clear increase in the DCR values with the bias voltage. This can be attributed to the fact that the bias voltage is often set so that it is close to the breakdown voltage at which the depletion region of the SiPM transitions into the breakdown. This can lead to an increase in dark count events as charge carriers are spontaneously generated without a photon falling on the detector. This increase increases with the OnSemi SiPM at high voltages, while an almost linear increase is visible with the other two. These differences are attributed to differences in the manufacturing technology as well as the design and structure of the SiPMs of the various manufacturers. With the Hamamatsu SiPM, an outlier occurs at 41 V. In direct comparison, the Broadcom SiPM has the lowest DCR values with a minimum value of 82.243 ± 0.651 kHz/mm^2 and a maximum value of 132.541 ± 1.050 kHz/mm^2 in the voltage interval under consideration. The Hamamatsu SiPM has the highest values, which are between 217.722 ± 2.049 kHz/mm^2 and 421.145 ± 2.859 kHz/mm^2 in the considered interval if the outlier is not considered. The OnSemi SiPM has values between 111.590 ± 0.884 kHz/mm^2 and 308.062 ± 2.441 kHz/mm^2. The DCR values specified by the manufacturer (table 1) are only outside the window under consideration for the Hamamatsu SiPM. For the investigation of single photon detection with SiPMs it is advantageous to have a low DCR, in this respect the Broadcom SiPM has the best values.

6.2.2 Comparison of crosstalk dependence on bias voltage

This section examines the dependence of the crosstalk probability on the bias voltage. The uncertainties are the same for all values under consideration and this absolute error has been determined in section 5.4. The values for the Broadcom AFBR-S4N66P024M SiPM is shown in Figure 37 for the OnSemi MICROFC-60035 in Figure 38, and the Hamamatsu S14160-6050HS in Figure 39.

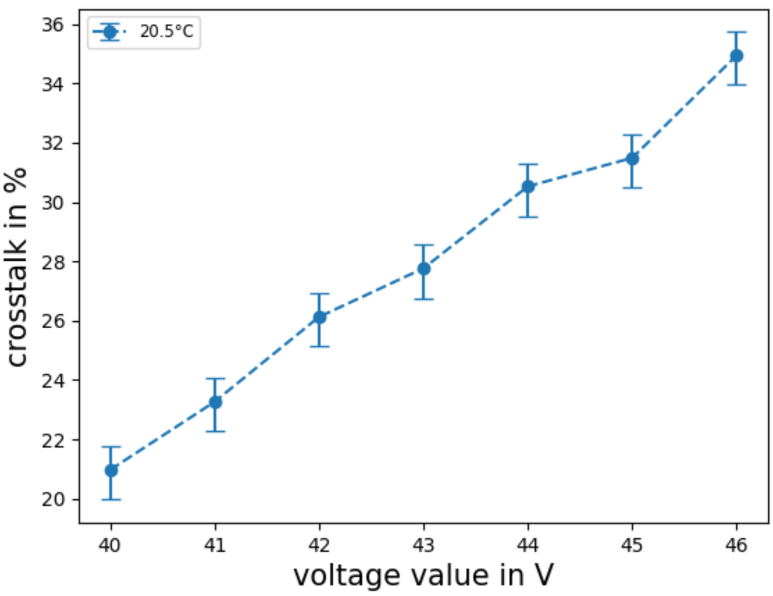

Figure 37: Crosstalk probability plotted against voltage for Broadcom AFBR-S4N66P024M SiPM.

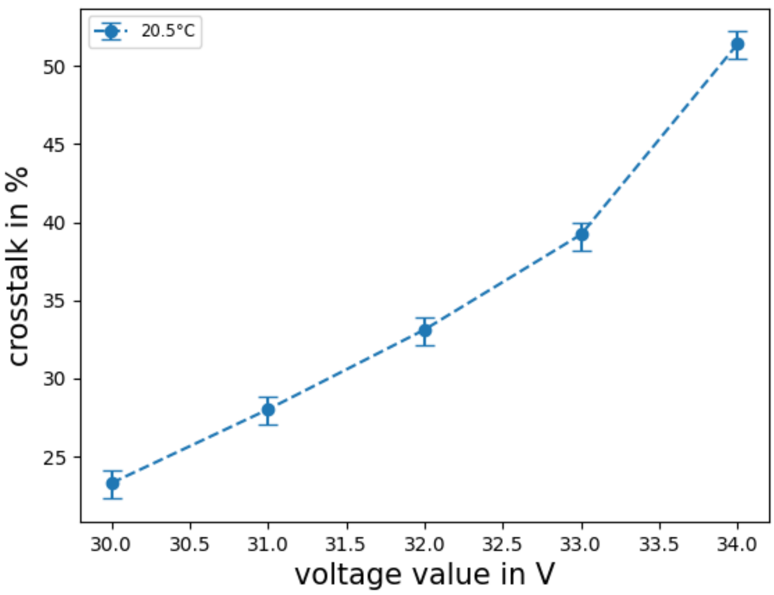

Figure 38: Crosstalk probability plotted against voltage for OnSemi MICROFC-60035 SiPM.

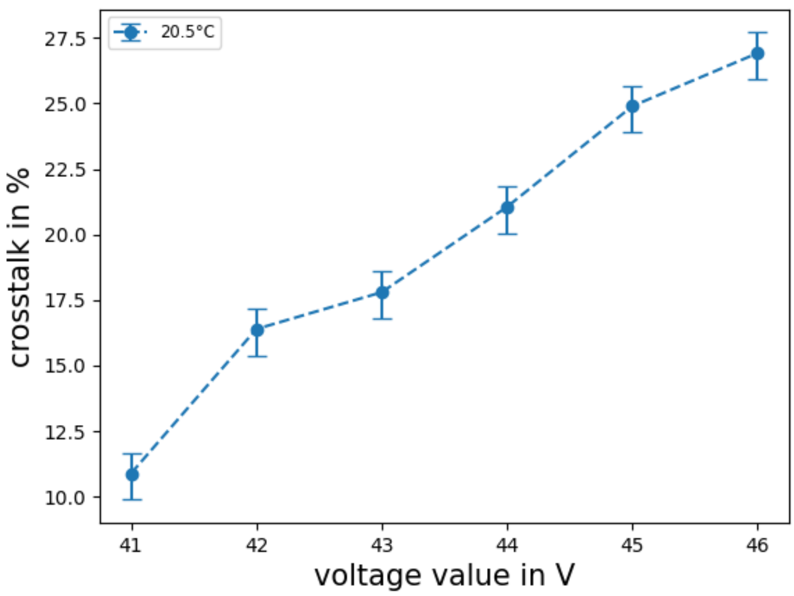

Figure 39: Crosstalk probability plotted against voltage for Hamamatsu S14160-6050HS SiPM.

For all three SiPMs, the crosstalk probability increases about linearly with the applied bias voltage. However, the OnSemi SiPM also shows a stronger increase towards higher voltages, which is attributed to the same reasons as when considering the DCR values. The Hamamatsu SiPM has the lowest crosstalk probability in the voltage interval under consideration, with a minimum value of 11,0 % and a maximum value of 26,9 %. The OnSemi SiPM has the highest crosstalk probability with values between 23.3 % and 51,4 %. The Broadcom SiPM had values between 21,0 % and 34,9 %. For the OnSemi SiPM, the crosstalk value specified by the manufacturer (table 1) is not within the considered voltage interval for the other two. Since it is also advantageous for single photon detection with SiPM to have a low crosstalk probability, the Hamamatsu SiPM performs best here.

6.2.3 Comparison of gain dependence on bias voltage

In this section, the dependence of the gain on the bias voltage is examined. As with crosstalk, an absolute error is assumed here for all values considered; this was determined in section 5.4 and is not mentioned further here. The values for the Broadcom AFBR-S4N66P024M SiPM are shown in Figure 40, for the OnSemi MICROFC-60035 in Figure 41, and for the Hamamatsu S14160-6050HS in Figure 42.

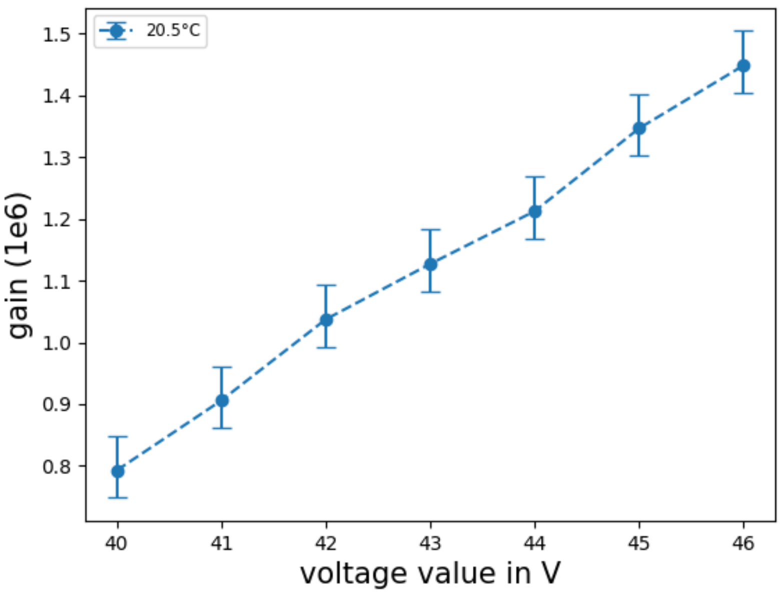

Figure 40: Gain plotted against voltage for Broadcom AFBR-S4N66P024M SiPM.

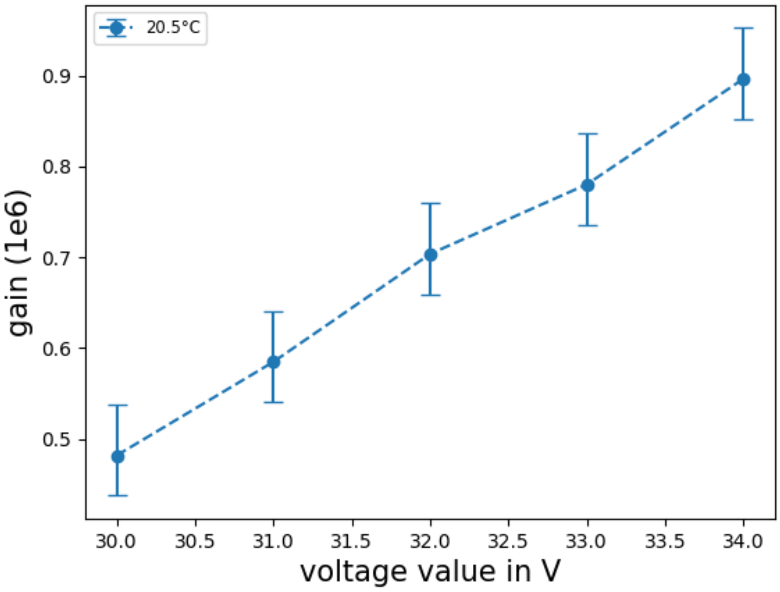

Figure 41: Gain plotted against voltage for OnSemi MICROFC-60035 SiPM.

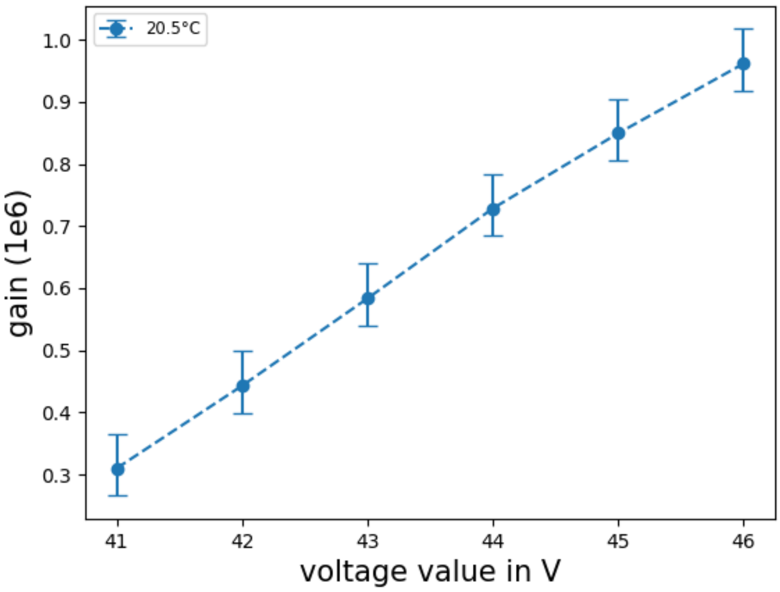

Figure 42: Gain plotted against voltage for Hamamatsu S14160-6050HS SiPM.

For all SiPMs, the gain increases almost linearly with the applied bias voltage. When a photon hits a SiPM, it generates electron-defect electron pairs due to the photoelectric effect. These charge carriers are accelerated by the electric field generated by the applied bias voltage. When they reach a critical voltage, they trigger an avalanche multiplication in which further charge carriers are generated. If the applied bias voltage is higher, this avalanche multiplication becomes stronger, which leads to a higher gain. The Hamamatsu SiPM has the lowest gain values. The Broadcom SiPM has the highest values with values between 0.792×10^6 and 1.449×10^6. The OnSemi SiPM and that of Hamamatsu have gain values in very similar ranges. For the OnSemi SiPM these are between 0.481×10^6 and 0.896×10^6 and for the Hamamatsu SiPM between $0.309 \cdot 10^6$ and 0.9616×10^6. The values for all three SiPMs in the measurements are significantly below the manufacturer's specifications (Table 1), which may indicate other analysis methods or other measurement circumstances of the manufacturer's measurements. For single photon detection with a SiPM, its gain must be sufficiently high to produce enough electrons to be able to measure the signal of individual photons. If the gain is too high, the SiPM may be overloaded, which can lead to saturation of the output signals. This means that the SiPM is no longer able to reliably detect and distinguish individual photon events, which reduces the measurement accuracy. However, the case that the gain is too high does not occur with any of the three SiPMs. Accordingly, the Broadcom SiPM comes out on top here as it has the highest gain values. Table 2 show a comparison of all values for the three SiPMs.

SiPM	DCR	crosstalk	gain
Broadcom AFBR-S4N66P024M	82.2 ± 0.651 kHz/mm^2 to 132.5 ± 1.1 kHz/mm^2	11,0 % to 26,9 %	0.8×10^6 to 1.4×10^6
OnSemi MICROFC-60035	111.6 ± 0.9 kHz/mm^2 to 308.1 ± 2.4 kHz/mm^2	23.3 % to 51,4 %	0.5×10^6 to 0.9×10^6
Hamamatsu S14160-6050HS	217.7 ± 2.0 kHz/mm^2 to 421.1 ± 2.9 kHz/mm^2	21,0 % to 34,9 %	0.3×10^6 to 1.0×10^6

Table 2: Comparison of DCR, crosstalk and gain of the investigated SiPMs.

7 Summary

In this bachelor thesis, the silicon photomultiplier (SiPM) AFBR-S4N66P024 from Broadcom, MICROFC-60035 from OnSemi and S14160-6050HS from Hamamatsu were characterized as potential candidates for a possible upgrade of the photocamera of the RICH detector at the CBM experiment. The SiPMs are characterized by parameters such as the dark count rate (DCR), crosstalk, afterpulsing, and gain. The SiPM is installed in a dark box that is as light-tight as possible and its temperature is controlled via a cooling system. The SiPM is then irradiated with ultra-short light pulses of 20 ps at a rate of 100 kHz. The signals are amplified via an amplification circuit and recorded with an oscilloscope.

Chapter 5 describes the analysis method for evaluating the signals and obtaining the values for DCR, crosstalk afterpulse, and gain. For this purpose, the signal is recorded once for 100 ns and once for 2000 ns. Using the signal recorded in a shorter interval, double photon and single photon treshold values are first determined to determine whether a signal peak corresponds to an avanche triggered by one or two photons. DCR, afterpulse, and crosstalk are determined using the peaks that lie above the specified tresholds. The gain correlates directly with the single photon equivalent signal value via a multiplicative factor. This analysis is performed for each SiPM for different temperatures and applied bias voltages. In the case of afterpulsing the inaccuracy of the measurements is too high to allow any conclusions. Due to this high error, afterpulsing is not taken into account in the following analyses. In a test for the reproducibility of the results, which was also carried out to determine the uncertainty of the DCR, crosstalk and gain values, it was found that the setup used has significant light pollution, which is due to the dark box not being sufficiently light-tight. As a result, a new setup was implemented with the room light switched off and a better sealed dark box. However, a dependence of the DCR of the crosstalk and the gain with the temperature of the SiPM was still carried out with the old setup.

The results are then discussed in Chapter 6. Since the setup with lower light pollution provides more accurate values, the absolute values for DCR, crosstalk and gain are also compared here to determine which SiPM is best suited for an upgrade of the RICH detector. It was found that the increase in DCR with increasing temperature was observed for all SiPMs. This increase is almost linear for the OnSemi and Hamamatsu SiPMs, while for the Broadcom SiPM the DCR increases more strongly with increasing temperature. The analysis of the dependence of the crosstalk values on temperature showed that the crosstalk values remain almost constant with increasing temperature for the same operating voltage for all three SiPMs. The gain values also remain almost constant with increasing temperature for each operating voltage for the Braodcom SiPM, while the Hammatsu SiPM and the show a slight decrease in gain values with increasing temperature. In the following, the dependence of the DCR, crosstalk and gain values on the bias voltage is investigated. For this purpose, the SiPM is installed in a dark box and a fixed temperature of 20.5 °C is set. For all three SiPMs, the DCR values increase by increasing bias voltages. This increases for the OnSemi SiPM at high temperatures, while an almost linear increase can be observed for the other two SiPMs. In this case, The Broadcom SiPM has the lowest DCR values with a minimum value of 82.2 ± 0.7 kHz/mm^2 and a maximum value of 132.5 ± 1.1 kHz/mm^2 in the voltage interval under consideration. Since it is advantageous to have a low DCR for the investigation of single photon detection with SiPMs, the Broadcom SiPM has the best values in this respect. The crosstalk probability increases for all three SiPMs with the applied bias voltage. However, the OnSemi SiPM shows a stronger increase towards higher voltages. The Hamamatsu SiPM has the lowest crosstalk probability in the voltage interval under consideration, with a minimum value of 11.0 % and a maximum value of 26.9 %. Since it is also advantageous for single-photon detection with SiPM to have a low crosstalk probability, the Hamamatsu SiPM performs best here. The gain of all SiPMs increases linearly with the applied bias voltage.

Accordingly, the Broadcom SiPM performs best here, as it delivers the highest gain values with values of 0.792×10^6 to 1.449×10^6. Based on this analysis and taking into account a price-performance ratio, a recommendation can be made for SiPMs of the type Broadcom AFBR-S4N66P024M for possible installation in the RICH detector compared to the other two SiPMs. It has low DCR values and an acceptable crosstalk of values between 20.9 % and 34.9 % and also delivers gain values that are within a reasonable range.

8 Appendix

8.1 DCR plots

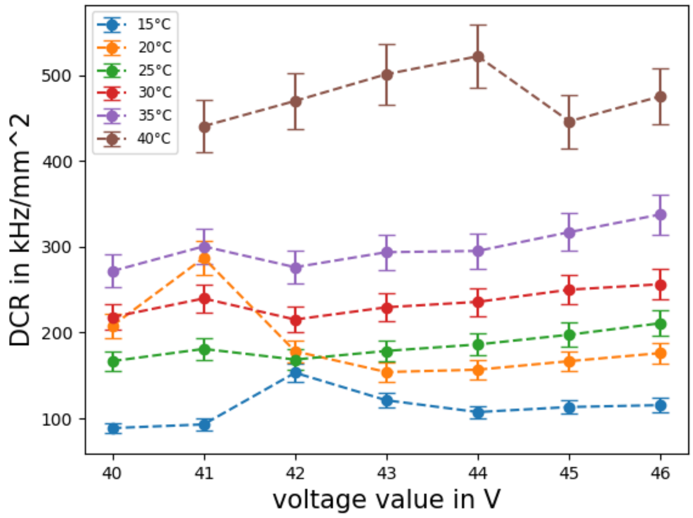

DCR plotted against voltage for Broadcom AFBR-S4N66P024M SiPM with old setup.

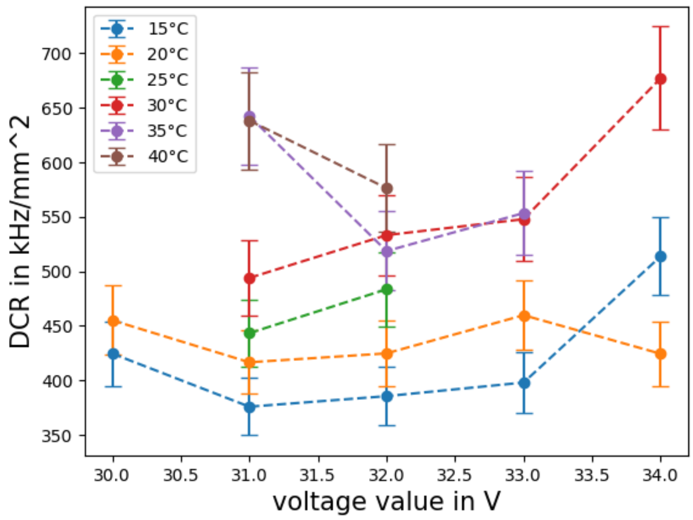

DCR plotted against voltage for OnSemi MICROFC-60035 SiPM with old setup.

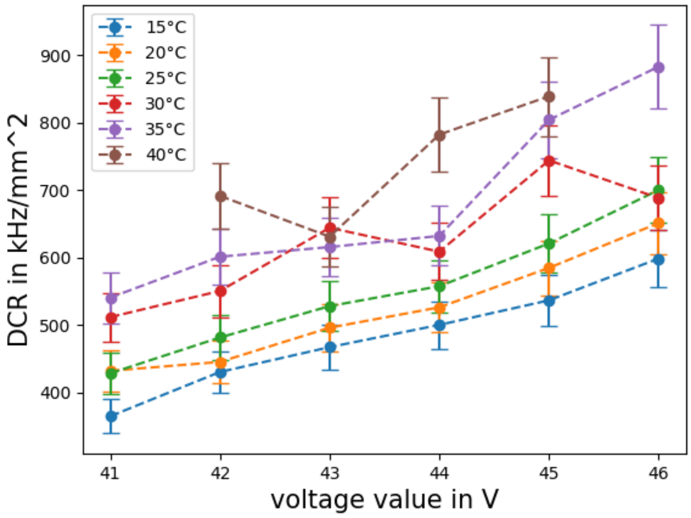

DCR plotted against voltage for Hamamatsu S14160-6050HS SiPM with old setup.

8.2 Crosstalk plots

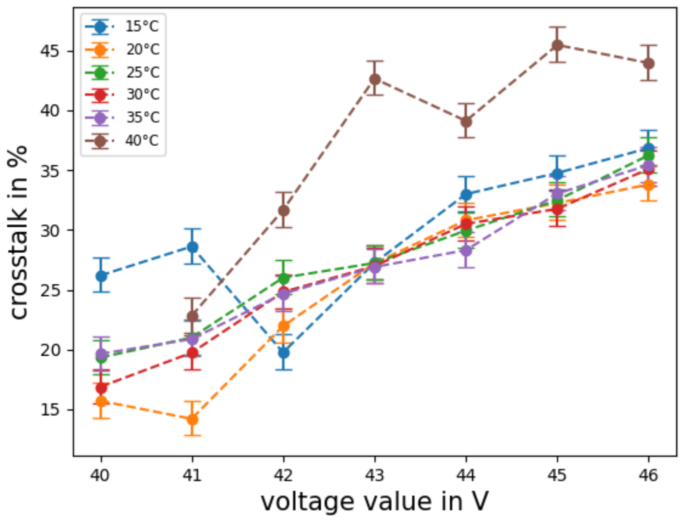

Crosstalk plotted against voltage for Broadcom AFBR-S4N66P024M SiPM with old setup.

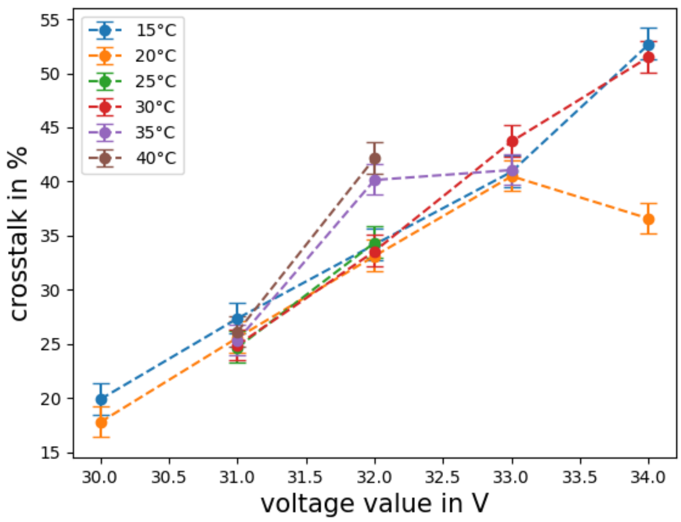

Crosstalk plotted against voltage for OnSemi MICROFC-60035 SiPM with old setup.

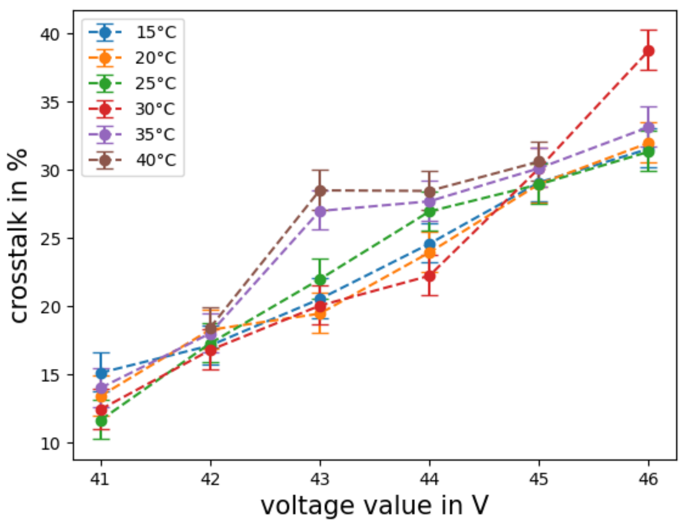

Crosstalk plotted against voltage for Hamamatsu S14160-6050HS SiPM with old setup.

8.3 Gain plots

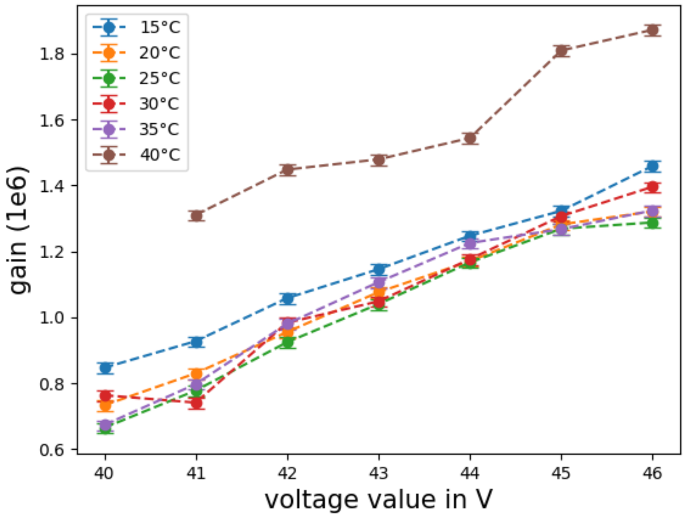

Gain plotted against voltage for Broadcom AFBR-S4N66P024M SiPM with old setup.

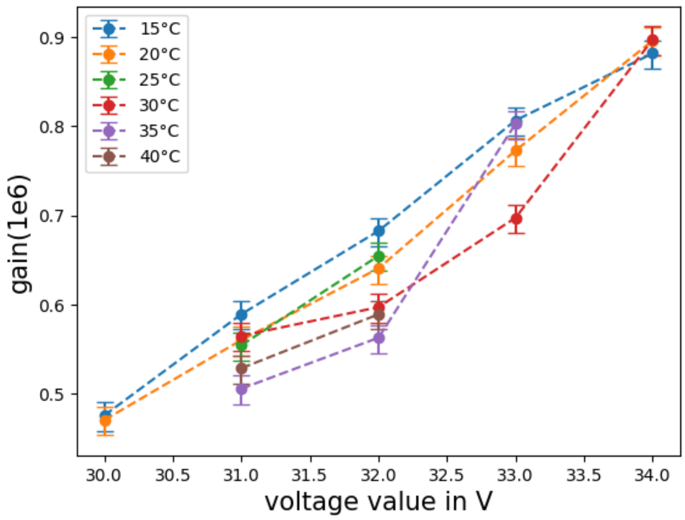

Gain plotted against voltage for OnSemi MICROFC-60035 SiPM with old setup.

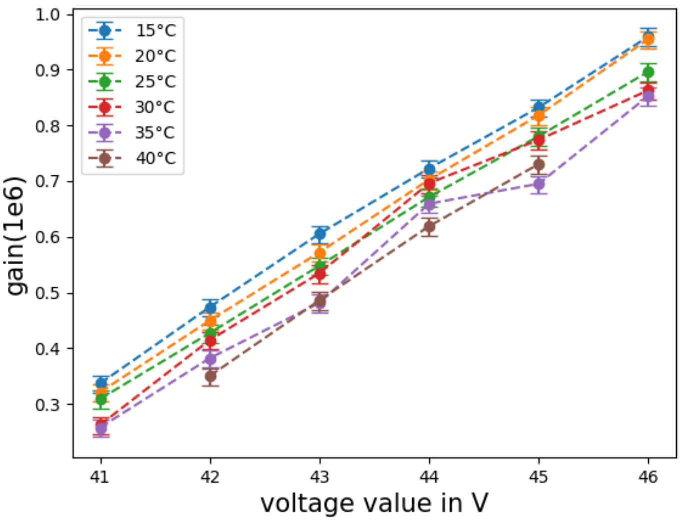

Gain plotted against voltage for Hamamatsu S14160-6050HS SiPM with old setup.

References

[1] www.gsi.de Compressed Baryonic Matter (CBM) (last retrieved 09.03.24)
https://www.gsi.de/work/forschung/cbmnqm/cbm

[2] www.researchgate.net Sketch of the proposed experimental setup for the CBM experiment (last retrieved 09.03.24)
https://www.researchgate.net/figure/Sketch-of-the-proposed-experimental-setup-for-the-CBM-ex fig1_228611863

[3] www.first-sensor.com Introduction to silicon photomultipliers (SiPMs) (last retrieved 13.03.24)
https://www.first-sensor.com/cms/upload/appnotes/AN_SiPM_Introduction_E.pdf

[4] electriciantraining.tpub.com Neets Module 07-Introduction to Solid-State Devices and Power Supplies (last retrieved 13.03.24)
https://electriciantraining.tpub.com/14179/css/Figure-3-3-Avalanche-Multiplication-119.htm

[5] Hilleringmann, UlrichSilizium-Halbleitertechnologie: Grundlagen mikroelektronischer Integrationstechnik. 5., erg. u. erw. Auflage. Vieweg + Teubner, Wiesbaden 2008. S.95 ff.

[6] hub.hamamatsu.com What is an SiPM and how does it work? (last retrieved 13.03.24)
https://hub.hamamatsu.com/us/en/technical-notes/mppc-sipms/what-is-an-SiPM-and-how-does-it-work.html

[7] www.schoolsobservatory.org Semiconductors (last retrieved 14.03.24)
https://www.schoolsobservatory.org/learn/tech/instruments/inst_ccd/semiconductors

[8] Lang, ThomasUntersuchen von Silizium Photomultipliern (SiPM) zur Verwendung in der Intensitätsinterferometrie. BA Thesis. Erlangen Centre for Astroparticle Physics Friedrich-Alexander-Universität Erlangen-Nürnberg. 2019

[9] www.gauss-centre.eu Numerical Determination of the Phase Diagram of Hadronic and Nuclear Matter (last retrieved 14.03.24)
https://www.gauss-centre.eu/results/elementaryparticlephysics/numerical-determination-of-the-phase-diagram-of-nuclear-matter0

[10] Reinecke, SaschaCharakterisierung von Spiegeln für den RICH-Detektor von CBM. Diploma thesis. Department of Mathematics and Natural Sciences Physics Department of the University of Wuppertal. 2011

[11] J. Adamczewski-Muscha, P. Akishin, K.-H. Becker , S. Belogurov, J. Bendarouach , N. Boldyreva , C. Deveaux , V. Dobyrn , M. Dürr , J. Eschke, J. Förtsch , J. Heep, C. Höhne, K.-H. Kampert, L. Kochenda , J. Kopfer , P. Kravtsov , I. Kres, S. Lebedevd, , E. Lebedeva , E. Leonova, S. Linev, T. Mahmoud, J. Michel , N. Miftakhov , W. Niebur , E. Ovcharenko, V. Patel , C. Pauly , D. Pfeifer , S. Querchfeld , J. Rautenberg , S. Reinecke , Y. Riabov , E. Roshchin, V. Samsonove V. Schetininh, O. Tarasenkovae , M. Traxlera , C. Ugura , E. Vznuzdaev , M. Vznuzdaev The RICH detector of the CBM experiment. Article. Nuclear Instruments and Methods in Physics Research A A 876 S.65-68. 2017

[12] CBM-WIKI.GSI.DE Grundlagen der Cherenkov Strahlung (last retrieved 20.03.24)
https://cbm-wiki.gsi.de/Public/CherenkovStrahlung

[13] WWW.SERAMARKOFF.COM Imaging Atmospheric Cherenkov Technique (last retrieved 20.03.24)
https://www.seramarkoff.com/2018/10/imaging-atmospheric-cherenkov-technique/

[14] DE.WIKIPEDIA.ORG Kohlenstoffdioxid (last retrieved 20.03.24)
https://de.wikipedia.org/wiki/Kohlenstoffdioxid

[15] GRUPEN, C.:Astroparticle Physics - "The Universe in the light of cosmic rays", engl. ¨Ubersetzung der dt. Originalausgabe, 1. Auflage, Springer-Verlag, 2005

[16] WWW.GAUSS-CENTRE.EU Numerical Determination of the Phase Diagram of Hadronic and Nuclear Matter (last retrieved 22.03.24)
https://www.gauss-centre.eu/results/elementaryparticlephysics/numerical-determination-of-the-phase-diagram-of-nuclear-matter0

[17] BALOG, TOMAS:Overview of the CBM detector system, GSI Helmholtzzentrum für Schwerionenforschung GmbH, Planckstrasse 1, 64291 Darmstadt, Germany, 2013

[18] E. HERING, K. BRESSLER, J. GUTEKUNST:Elektronik für Ingenieure und Naturwissenschaftler. Springer, 2005

[19] DE.WIKIPEDIA.ORG Standard error (last retrieved 25.03.24)
https://en.wikipedia.org/wiki/Standard_error

[20] C. JACKSON, K. O'NEILL, L. WALL, B. MCGARVEY:High-volume silicon photomultiplier production, performance, and reliability, SensL, 6800 Airport Buisness Park, Cork, Ireland, 2014

[21] WWW.ONSEMI.COM Introduction to the Silicon Photomultiplier (SiPM) (last retrieved 25.03.24)
https://www.onsemi.com/pub/Collateral/AND9770-D.PDF

[22] J. PEÑA-RODRÍGUEZ, C. PAULY, AND K.-H. KAMPERT:SiPM electronics readout for the Ring Imaging camera of the CBM experiment, Fakultät für Mathematik und Naturwissenshaften, Bergische Universität Wuppertal, Germany, as part of CBM progress report 2024

[23] WWW.RESEARCHGATE.NET Ring Imaging Cherenkov Detectors: The state of the art and perspectives (last retrieved 26.03.24)
https://www.researchgate.net/publication/234222993_Ring_Imaging_Cherenkov_Detectors_The_state_of_the_art_and_perspectives/link/5508524a0cf27e990e0a31ba/download

[24] CBM-WIKI.GSI.DE CLAUDIA HÖHNE:Grundlagen des RICH Detektors (last retrieved 26.03.24)
https://cbm-wiki.gsi.de/Public/RichDetektoren

Acknowledgements

First of all, I would like to thank **Prof. Dr. Karl-Heinz Kampert** for making it possible for me to write my Bachelor's thesis in the Astroparticle Physics department. I would also like to thank **Prof. Dr. Christian Zeitnitz** for volunteering as the Co-Corrector for this thesis.

I would also like to thank **Dr. Christian Pauly** and **Dr. Jörg Förtsch** for their help in finding a topic for the thesis and active support in evaluating the data and writing the thesis.

Special thanks go to **Dr. Jesús Peña Rodríguez** for his help with problems during data collection, analysis and for being available for questions at any time.

Finally, I would like to thank the entire Astroparticle Physics working group at the University of Wuppertal. There is a very nice working atmosphere and there was always someone available to answer questions.